Imaging Au nanocrystals with Coherent X-ray Diffraction Imaging

Loren James Beitra

London Centre for Nanotechnology and
Department of Physics and Astronomy
University College London

l.beitra@ucl.ac.uk

Supervisor
Prof. Ian K. Robinson

September, 2010

Abstract

Coherent x-ray diffraction imaging is a remarkable tool, which allows the very structure of nanocrystals to be examined in a unique way. This report summarises the progress made so far in investigating Au nanocrystals with CXDI and includes discussion of the principles of CXDI, iterative phase retrieval methods and sample preparation. The results from experiments are described and interpreted: laser induced heating of Au nanocrystals, visualising FIB damage and examining crystallographic imperfections in Au with multiple Bragg peak CXDI.

Table of Contents

Title Page 1

Abstract 1

Chapter 1 - Introduction 3
- Some Applications of Gold 4
- Properties and Crystal Structure 6
- Surfaces 7
- Imperfections in Au 8
- Plastic deformation 9
- Slip 10
- Twinning 12

Chapter 2 – The physics of Crystal Growth 13
- Heterogeneous nucleation 15

Chapter 3 – Sample preparation 17
- E-beam prepared patterned Au samples 17

Chapter 4 – Coherent X-ray Diffraction 20
- X-ray Diffraction: revealing crystal structures 20
- Coherent X-ray Diffraction Imaging (CXDI) 22
- Oversampling 24
- Coherence 24
- Transverse Coherence 25
- Longitudinal Coherence 26
- Phase Retrieval 28
- Error Reduction (ER) 30
- Hybrid Input Output – HIO 32
- Shrinkwrap vs. Box Supports 33
- Displacement Field 35

Chapter 5 - Experiments and Reconstructions 38
- Basic Experiment Procedure 38
- Confocal Microscope Alignment Method: measuring crystals multiple times[30] 40
- Finding a Bragg peak 41
- Measurement Settings 42
- Effects of Laser induced heating of Au crystals 43
- Experimental Method 44
- Results 45
- Summary 51
- Visualising FIB induced damage with CXDI 52
- Experimental Method 52
- Results 54
- Summary 57

Study of crystallographic imperfections with CXDI 57
Results 58
Displacement field from three Bragg reflections 62
Summary 63

Chapter 6 - Conclusions 65

Chapter 7 – Future work 68

References 69

Chapter 1 - Introduction

Gold is ensured a permanent place in human history as one of the most important substances known to man. Since the beginning of recorded history, gold has played a vital role in every major culture around the world, coming to symbolise wealth and power in the hands of the rich. Known as both the “King of Metals” and “noble”[1], its beauty, malleability and resistance to chemical reaction go some way in explaining the extraordinary lengths humans have gone to in order to obtain it. It is the most ductile and malleable of metals allowing it to be mechanically worked to high precision[2]. Its unusual optical nature giving rise to a deep yellow colour, (caused by relativistic a small band gap between two electron orbital’s[1]) which hints at some of its interesting properties. This chapter will introduce some of the remarkable and exciting properties of gold, the main material of interest in this report.

Figure 1. A Natural gold nugget weighing 0.47kg found in Australia

Some Applications of Gold

Its mechanically soft, yet chemically robust properties make gold something of an oddity. Historically, bulk gold has been found to be most useful for decorative purposes and interestingly, on the nanoscale it was used as long ago as the 10th century to colour stained glass. In recent years high electrical and thermal conductivity have found gold used in many applications in the electronics industry. On the scale of nanometre sized integrated electronic devices, its weak resistance to oxidation compared to silver, and its relatively low cost in comparison with platinum, make it highly useful for application as electrodes and wires in nanoelectronics[3]. It has also seen many applications in medicine and the pharmaceuticals industry partly due to a high resistance to bacterial colonization and as a result is used in many implants in the body at risk of infection[3].In the field of particle based tumour treatment, it was reported that radioactive colloidal gold nanoparticles have been used successfully as a treatment for liver cancer and sarcoma[4]. It was also reported that Au nanoparticles, stabilized by 5-aminovaleric acid, were used to selectively and rapidly penetrate into cancer cells. The success of such treatment methods have been attributed to the ability of gold nanoparticles to accumulate in tumours[5]. It has also found uses in immunodiagnostics (diagnosis of disease based upon antigen-antibody reactions (antigen any substance which causes the production of antibodies))[4] and targeted drug delivery.

As recently as the 1980's, another unexpected use of gold was discovered when it was found that very small gold nanoparticles could act as a catalyst in low temperature reactions. Despite its perceived nature as an unreactive metal, when small enough, it can act as one of the most reactive catalysts[6]. Remarkably in 1987, Haruta et al. found that gold could be used as a catalyst in CO oxidation as low as 70ºC, which had far reaching industrial and environmental implications. The nanoparticles prepared from an aqueous solution of gold chloride acid, showed that gold is perhaps one of the most interesting metals in terms of use in catalysis[6, 7]. It was also shown in the mid 80's that gold acts as a powerful catalyst for acetylene hydrochlorination[8].

Gold also finds application as an optical material especially because it reflects infrared very well. It is therefore commonly found in heat shielding in heat resistant suits and visors, including those used by astronauts in space. In order to adequately protect against solar radiation in space, the wavelength range of interest is between 0.2 and 15 microns, making gold an appropriate choice. A semi-transparent film with thickness of 50nm is used in spacesuit visors[9].

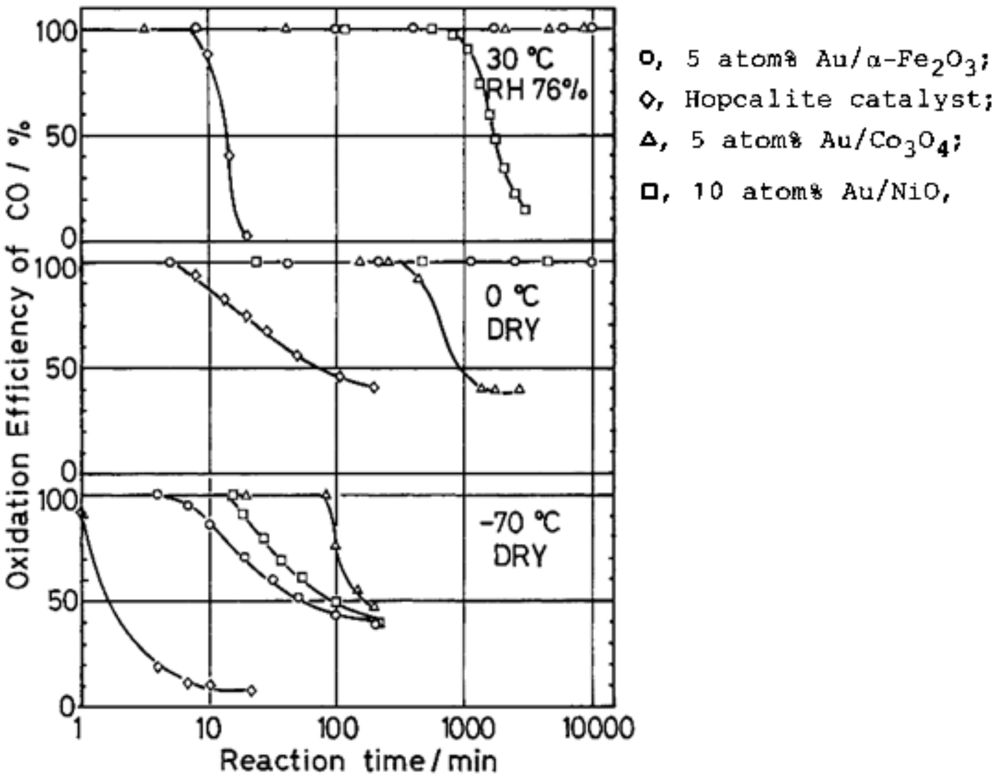

Figure 2. Oxidation efficiently of CO as a function of time with Au catalyst of different sizes on different oxide substrate[7].

Properties and Crystal Structure

Gold is a 'noble' metal element Z=79 and has one stable isotope with atomic mass 197. It is not only the 'noblest' of metals resisting oxidation and corrosion to a greater extent than any other, having the highest oxidation potential, but it also has the highest electron affinity of any metal i.e. resisting ionisation[1]. Gold, in a stable state, at low temperature and standard pressure, is found to occur in the Face-Centre-Cubic structure, therefore 4 atoms per unit cell. At high pressure it can occur in a hexagonal close packed phase when above 180GPa. Each gold atom is surrounded by 12 equidistant atoms with cell spacing of 0.408nm and nearest neighbour distance of 0.2884nm. It belongs to space group Fm3m [10]. The spectacular yellow colour of gold is due to a small band gap between the full 5s band and the half full 6s band, the small size of which (relative to classical electron configuration explanations) can be accounted for with relativistic effects[1]. The high malleability of gold can be accounted for by the high number of glide planes in its structure, as well as a high atomic mobility.

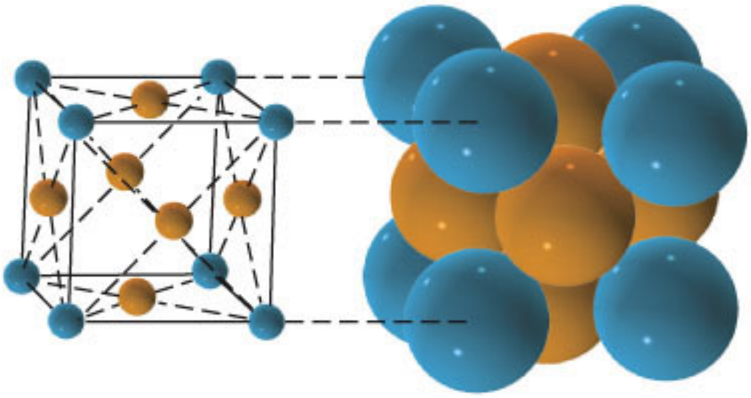

Figure 3. The Face Centre Cubic crystal structure[11]

Surfaces

Far from being unreactive and inert, the surface of gold has been found to react strongly and favourably with some anions and favour the formation of self assembled monolayers (SAM's). The reaction on a gold surface with sulphur based molecules is especially active[1]. The surface lattice of gold is arranged in FCC lattice formation just like in the bulk material.

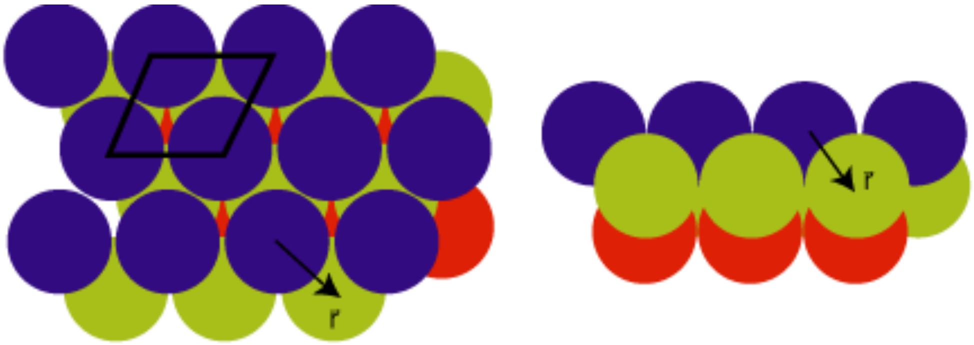

Figure 4. {111} surface of fcc crystal seen from above (left) and from the side (right)

Surface close packing is the highest for the {111} surfaces and is shown in Figure 4. The coordination number for the surface of {111} is 9 therefore for gold the number of broken bonds are 3 per atom. The cohesive energy, E_C, (which describes the energy necessary to break an atom completely free from a solid) is $E_C/4$ for the {111} surface unit cell[12]. Sulphur based SAM's are able to bond strongly to the surface of gold because of these broken bonded atoms, which no longer share the full 12 neighbouring Au atoms. This reaction with sulphur-based molecules remains confined to the outermost layers of the crystal. However, reactions of this type in other noble metals such as silver will travel further into the crystal.

Consequently, gold is easily cleaned of contaminants and can be relied upon to be uncontaminated at its core whereas silver is easily tarnished[1].

Like most surfaces of 5d electron transition metals, Au reconstructs i.e. surface atoms assume a slightly different 2d surface structure due to altered interatomic energies than the bulk. In order to account for the broken bonds at the surface, this manifests itself by increasing the actual coordination number of each atom in the surface sheet. It is also thought that this may be as a result of relativistic electron configuration effects. Figure 5 shows reconstruction on the surface of an Au (111) with characteristic herringbone appearance. This is due to a uniaxial compression of this surface layer. The result of which is that surface structure, with respect to the second layer of atoms, transitions between FCC-Bridge sites-HCP-Bridge sites-FCC. This structure transition causes periodic oscillations in contour level at the surface, which can be seen in Figure 5. This formation reduces the elastic strain energy at the surface layer[12] and crucially with respect to chemical interactions taking place on the surface, increases the surface area to volume ratio of the crystal [?].

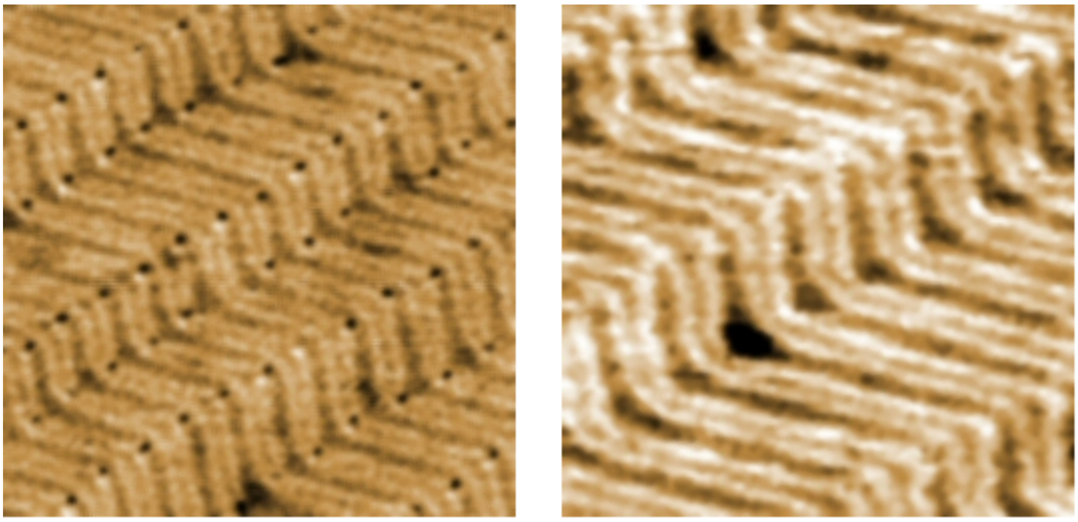

Figure 5. STM picture of Au (111) herringbone reconstruction at room temperature (left) and 394ºK (right)

Imperfections in Au

Crystalline structures are often tactically discussed in terms of perfect structure. In practice, however, all except ultra-nanoscale crystals contain defects and imperfections in their makeup. Many experimental techniques can be used in order to locate and identify such defects in the hope of understanding their nature. Often, defects are purposefully introduced into a material in order to finely tune its properties. This is known as strain hardening[13]. One such example of this is the introduction of defects into a metal tool by rapid heating and quenching in order to give it a specific different degree of flex and hardness. Too much work hardening and the tool will become brittle and liable to fracture. It has been found that the strain-hardening rate is closely dependent on particle diameter. As crystal diameter decreases, its dislocation density decreases, so when stress is applied, more is required to cause a defect. This is because the smaller a crystal is, the fewer sites there are available for a defect to occur at [14].

Plastic deformation

Strength and ductility are two properties strongly controlled by atomic structure and this section will discuss the *plastic* and *elastic* deformation of macroscopic single crystals before moving onto atomic scale imperfections in the next sections[15].

The mechanical properties of many materials can be determined by performing simple laboratory based stress-strain experiments. The most common of these tests are tension, compression, and shear/torsional tests[13]. An applied stress, when less than the elastic limit of the material, will cause deformation, which is said to cause elastic deformation, so when the stress is removed, the sample will return to its original configuration. If applied stress is greater than or equal to the yield stress, the material will undergo unrecoverable plastic deformation. On a finer scale, after an elastic loading regime, the metal will exhibit discrete bursts of yielding. It has been found that compressive yield stress scales as the inverse square root of particle diameter, d so $\sigma \propto \frac{1}{d^2}$ [14]. Shear stress (rather than tension or compression, σ), τ has the relation

$$\tau = G\gamma \tag{1}$$

where G is the shear modulus (simply the ratio between shear stress and shear strain) and γ is the shear strain[15].

If a stress is applied to a crystal, the atoms will be displaced from their equilibrium lattice positions. This elastic displacement from the ideal position can be observed experimentally with x-ray methods such as CXDI. Irreversible, plastic deformation of atoms within a metallic crystal occurs primarily by four mechanisms; slip, twinning, grain boundary sliding and diffusion. Slip is the dominant mechanism to be discussed as the other three occur predominantly at low temperature in HCP metals and at high temperature respectively[15].

Slip

The bending of a metal ruler by a large angle will cause grains, visible to the naked eye to appear across its surface. Closer examination of these grains under a powerful microscope will reveal that each grain consists of a series of parallel lines, which are a consequence of slip, a mechanism by which two crystal regions glide across each other. These lines are visible examples of surface stress relief due to slip[15]. Atomic dislocations such as these move along a set of preferred planes in a given crystal structure known as the *slip plane*. On the preferred plane there are specific directions, which dislocations will move along, called the *slip direction*. The combination of *slip plane* and *slip direction* is called a *slip system[13]*. Slip systems can range vastly in size from one atomic plane's width to sections larger than 0.69µm in breadth according to one STM based study[16]. It has also been reported that there is a critical crystal size of 15nm above which slip is still the dominant deformation mechanism of plastic deformation[17].

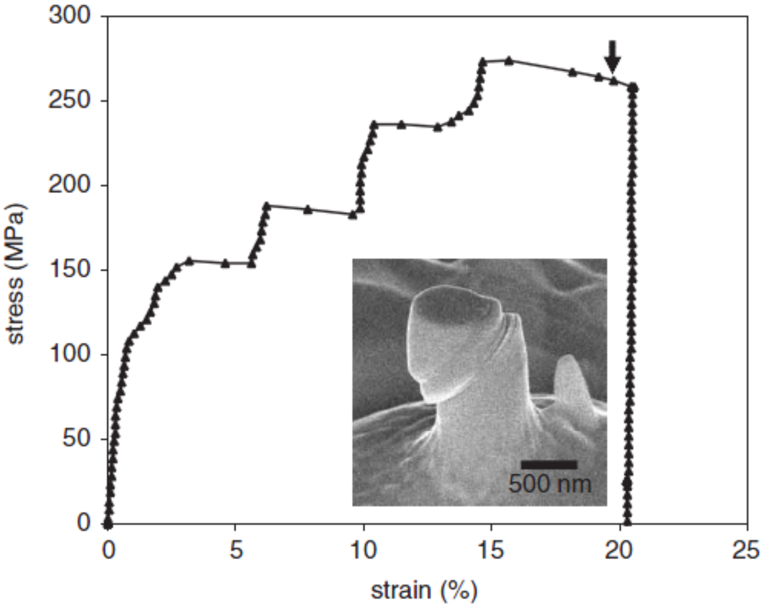

Figure 6. Engineering stress-strain diagram from experimental study carried out by compressing a 710nm diameter gold column. An initial elastic deformation section is followed by a flat plastic deformation plateau, which is then followed by another section of elastic deformation. Plastic deformation in the form of slip can be seen to occur in discrete steps as shown in the SEM image alongside.

F Measurements on crystals with a known crystallographic orientation have revealed that in fcc crystals, slip occurs along {111} planes and in the <110> directions. Since there are four unique (111) sets each with three slip systems (e.g. (111)[-110], (111)[10-1] and (111)[0-11]) we know that fcc crystals have 12 slip systems [15]. The large number of slip systems in fcc crystals helps to explain their relative ductility when compared with their hcp counterparts[13].

If a tensile or compressive stress is applied to a crystal, stress in the slip direction, along the slip plane will be a shear component of the tensile stress, unless it is parallel or perpendicular to the direction of application. We can resolve the magnitude of this shear stress component by considering the angle ϕ, between the normal to the slip plane and the direction of applied stress, and a second angle, λ between slip direction and direction of applied stress[13]. This is illustrated in Figure 7 diagrammatically. The resolved shear stress, τ_R is

$$\tau_R = \sigma \cos\phi \cos\lambda \qquad (2)$$

where σ is applied stress or Force/Area

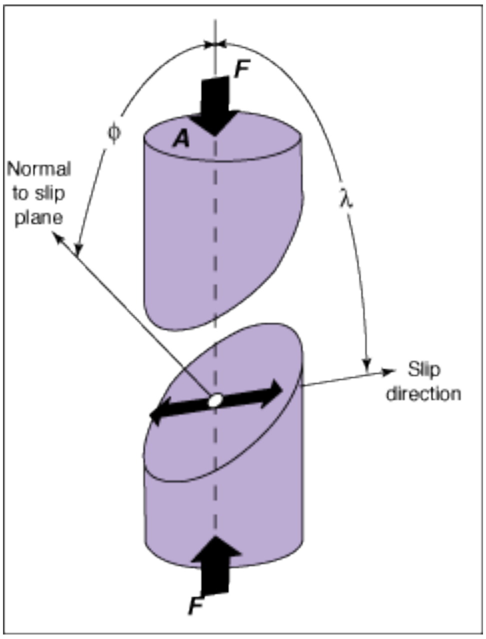

Figure 7. Diagram showing direction of force along tensile axis, direction of slip and direction normal to slip plane along with geometrical relationships [18].

One slip system will generally be oriented more favourably for slip to occur along it i.e lowest value to cause yielding at $\gamma = \phi = 45^\circ$ so has the largest resolved shear stress. At $\gamma = \phi = 45^\circ$, [13] as a result of the $\cos^2 u = \frac{1}{2}$ identity we get an expression for the minimum stress to cause a yielding event of

$$\sigma_{min} = 2\tau_{R\ max} \qquad (3)$$

Twinning

If the crystallographic stacking sequence is changed in an fcc metal, we will get a ‘twin boundary’ between the two sections of different stacking sequence. The section of crystal with alternate stacking is called a twin. A phenomenon similar to this has been seen in several reconstructions from CXDI data (chapter 7) therefore it is important to understand the nature of this twin boundary. Twin crystals can form in several ways for example during crystal growth (in the case of our samples during initial annealing or as a result of recrystallisation after laser induced heating) or also due to deformation caused by strain. Crystalline twinning can act as a mode for plastic deformation[15]. It is worth noting that slip usually occurs more often in metals than twinning and that deformation twinning is rare in fcc metals and occurs mostly at low temperature[15].

Chapter 2 – The physics of Crystal Growth

Nucleation

The freezing of liquid metal to form a single crystal about a nucleation point is a remarkable process in which a small number of atoms arrange themselves into an ordered structure as a result of a change in the Gibbs free energy ΔG. It involves what is arguably the most important phase transition because almost all metals used for a practical purpose will go through this transformation[15] resulting in a material with very different physical and chemical properties[13]. Like most phase transformations, the solid-liquid transition does not occur instantaneously, but starts with nucleation at a single point and the formation of a stable pair of atoms, or dimer[19]. We will see that nucleation can be of two types: heterogeneous and conversely homogeneous (The Greek heteros meaning different and homos meaning the same), the difference being the location at which nucleation occurs.

Homogeneous Nucleation

Nucleation occurs much less readily in the interior of a uniform substance where the new phase must form in the bulk of the parent phase. The classical theory of nucleation involves consideration of the total free energy ΔG, which is an important thermodynamic function with respect to phase transitions. It consists of two parts; the volume free energy and surface free energy. A transformation will occur only when this has a negative value. The volume free energy contribution upon freezing is simply $\Delta G_V = G_s - G_l$, where G_s and G_l are the free energies of solid and liquid. As the liquid is cooled, G_l will become smaller until below the equilibrium solidification temperature, at which G_V will become a negative value. If the liquid is cooled below the freezing point by ΔT without freezing, supercooling has occurred. In order to explain this phenomenon of a supercooled liquid, we must also take into account the contribution of surface free energy, which effectively acts as a barrier to freezing. When a solid nucleus (assumed to be a sphere) first forms in a bulk liquid, it is extremely small in size and as a result the surface to volume ratio is very high; so, at the start of the freezing process, contributions from the surface are the dominant factor. When both the volume and surface free energies are taken into account we can write the total change in free energy to form the solid nucleus as

$$\Delta G = \frac{4}{3}\pi r^3 \Delta G_V + 4\pi r^2 \gamma \tag{4}$$

For pure materials, where γ is the surface free energy. The first term corresponds to the contribution from the volume of the particle and thus decreases to the third power of r. The second term is the surface term and thus increases with the square of r. It is useful to plot these terms, along with their sum and this is shown in Figure 8.

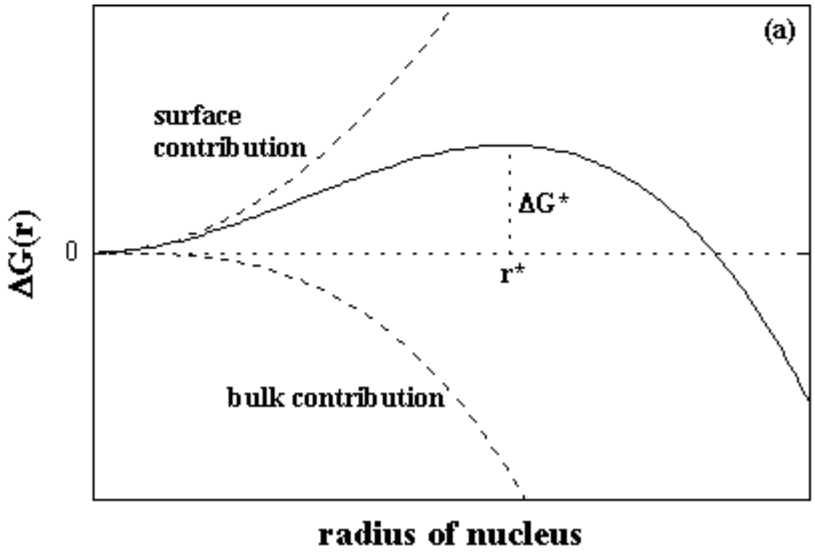

Figure 8 Nucleation free energy ΔG as a function of the cluster radius r. Classical nucleation theory explains the ΔG as the sum of the surface contribution and the volume contribution. [20]

If a solid *nucleus* forms within a liquid, its free energy will first increase until a critical point (r*), beyond which the free energy will begin to decrease[13]. The energy change required to reach this point is known as the activation free energy. Once this barrier has been overcome the nucleus is termed an *embryo*[13]. An interesting question is at which size this transition will occur. The differential of Eq. (5 set to zero at r = r* allows us to find the expression for this critical particle radius.

$$r^* = \frac{-2\gamma}{\Delta G_V} \tag{5}$$

Substitution of this r* for r in Eq. (4 gives

$$\tau = \frac{4\pi}{3}\left(\frac{-2\gamma}{\Delta G_V}\right)^3 \Delta G_V + 4\pi\left(\frac{-2\gamma}{\Delta G_V}\right)^2 \gamma \qquad (6)$$

Factorising by 4πr* gives

$$\Delta G = 4\pi\left(\frac{-2\gamma}{\Delta G_\tau}\right)^2 \left(\frac{-2\gamma}{3} + \gamma\right) \qquad (7)$$

Then expanding the brackets we get an expression for the activation free energy G*

$$\Delta G^* = \frac{16\pi\gamma^3}{3(\Delta G_V)^2} \qquad (8)$$

When the activation free energy is a negative quantity, the nucleation is favoured in the system.

Heterogeneous nucleation

Nucleation will occur much more frequently as heterogenous nucleation, where atoms cluster together at a nucleation site such as a pre-existing interface or an impurity. The process of heterogeneous nucleation will now be discussed by considering nucleation of a new phase, β our of the parent phase which we will call α in a substrate. The heterogenous nucleation energy, ΔG^*_{het} is dependent on a geometrical factor, $f(\delta)$ determined by the contact angle, δ between α and β. Figure 9 illustrates the meaning of the contact angle. $f(\delta)$ is given by

$$f(\delta) = \frac{(1-\cos\delta)^2(2+\cos\delta)}{4} \qquad (9)$$

and

$$\Delta G^*_{het} = \Delta G^*_{\text{hom}} \cdot f(\delta) \qquad (10)$$

$$\Delta G^*_{het} = \left(\frac{16\pi\gamma^3}{3(\Delta G_v)^2}\right) f(\delta) \qquad (11)$$

where $f(\delta)$ is a value which varies from 0 to 1 as the contact angle, δ varies from 0° to 180°. As a result $\Delta G^*_{het} < \Delta G^*_{\text{hom}}$ meaning less energy is required in heterogeneous nucleation.

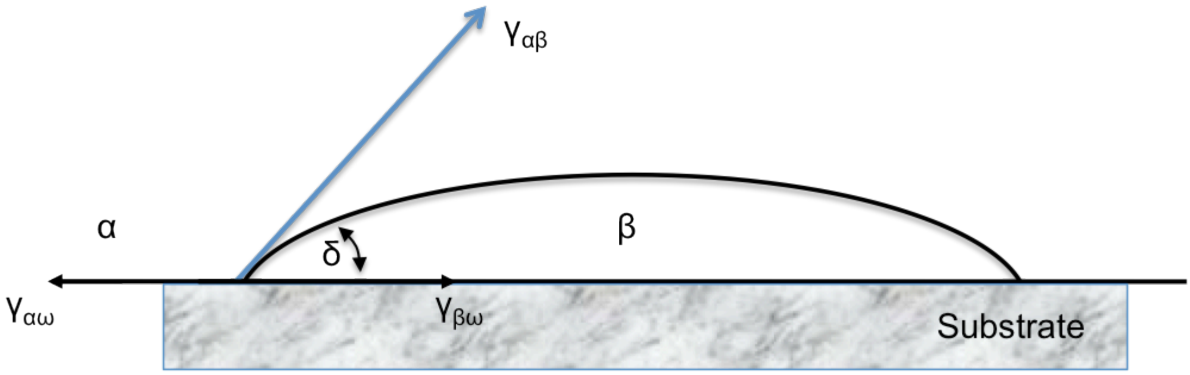

Figure 9. Surface tension diagram showing nucleation on substrate

Once the first crystal forms (the nucleus), it acts as a site for crystalisation to occur. Successive layers of atoms

Chapter 3 – Sample preparation

This section will discuss the design and preparation of samples used in our CXDI experiments. The method of ebeam lithography will be briefly explained before an in-depth discussion of sample design.

In the typical CXDI experiment, a sample consisting of a blanket coating of nanocrystals on a substrate will be placed on a diffractometer. The coherent x-ray beam is then used to illuminate the sample and x-rays scattered from crystals can be measured on a detector. The ability to determine precisely which crystal the scattered x-rays originate from is quite an obvious advantage. This allows multiple measurements to be made from the same nanocrystal at a later date, so opening up the possibility of measuring a crystal before and after some change is caused in order to study the effects. A set of patterned Au on SiO2 samples used in conjunction with a confocal alignment microscope in situ at the synchrotron beamline, made this a reality. The patterned samples created were useful for several reasons, which will be discussed in this chapter. Primarily, it made it possible to measure isolated crystals allowing us to be certain of which crystal was being measured at any time. This would have not been possible without the confocal alignment microscope. The alignment method is briefly as follows: firstly, with the aid of the confocal and a phosphor screen, the x-ray beam is aligned with the known diffractometer centre of rotation in all three dimensions. Next, the confocal height is adjusted such that the sample appears in focus through the microscope. This confocal focal height is then kept static and used as a reference point. We can now be certain that provided a crystal of interest is placed into the known centre of rotation and the sample appears in focus, then the crystal of interest is in the x-ray beam.

E-beam prepared patterned Au samples

A set of patterned Au on SiO2 samples were prepared by Nao Shimamoto from Waseda University, Japan. The samples were prepared with use of e-beam lithography whereby a precise pattern can be ‘printed’ onto a substrate in the material desired. These film samples were then high temperature annealed in order to produce single Au nanocrystals.

The samples consisted of a series of small Au film dots of different shapes and sizes. By varying the shape and sizes of the film dots, we hoped to be able to control the final crystal properties such as shape, size, alignment and probability of twin crystals. Figure 9 shows the schematic of the first sets of samples produced and a close-up SEM image of a triangular film. They consist of 9 squares each of which contains an array of hundreds of Au film dots. The film shapes chosen were triangle, hexagon and square, and film dot areas were 1μm^2, 0.25μm^2 and 4μm^2. It was found that the best thickness of Au film to use is between 15 and 25 nm thickness.

It was found that samples with a 3nm Chromium or Titanium layer on the substrate improved crystal adhesion to the sample. When a Bragg reflection is being measured it is not unusual for the crystal to shift completely out of the path of the beam during measurement. The flux of the focussed x-ray beam imparts such a large amount of energy that this additional adhesion is of great benefit during experiments.

Film dot shape has been found to have some effect on alignment and the number of crystals resulting from an annealed film dot. Rhombus film patches are much more likely to produce multiple crystals than triangle or hexagonal.

Film dot size plays a crucial role in the resulting crystals. The larger the film dot the more crystals will be formed after annealing. With a 4 micron area film dot, 2 or more crystals will be formed routinely whereas 0.25 micron area dots will almost never form multiple crystals.

Figure 9c shows some crystals formed after high temperature annealing of 0.25 micron area triangular Au film dots. The crystals have all aligned to the edges of the triangular shape. The outline of the initial triangular pattern can be seen on the substrate due to different substrate oxidation amounts – one theory is that the faster the crystal forms in the furnace, the more time the substrate has exposed to atmosphere at high temperature.

A new set of samples is going to be produced to be used in a future experiment at the LCLS (linear coherent light source), which is an XFEL (x-ray free electron laser). We will require a large number of extremely similar crystals in this experiment because each x-ray pulse will destroy the crystal being imaged. As a result, the more similar the crystals to one another the easier analysis of results obtained in this experiment will be.

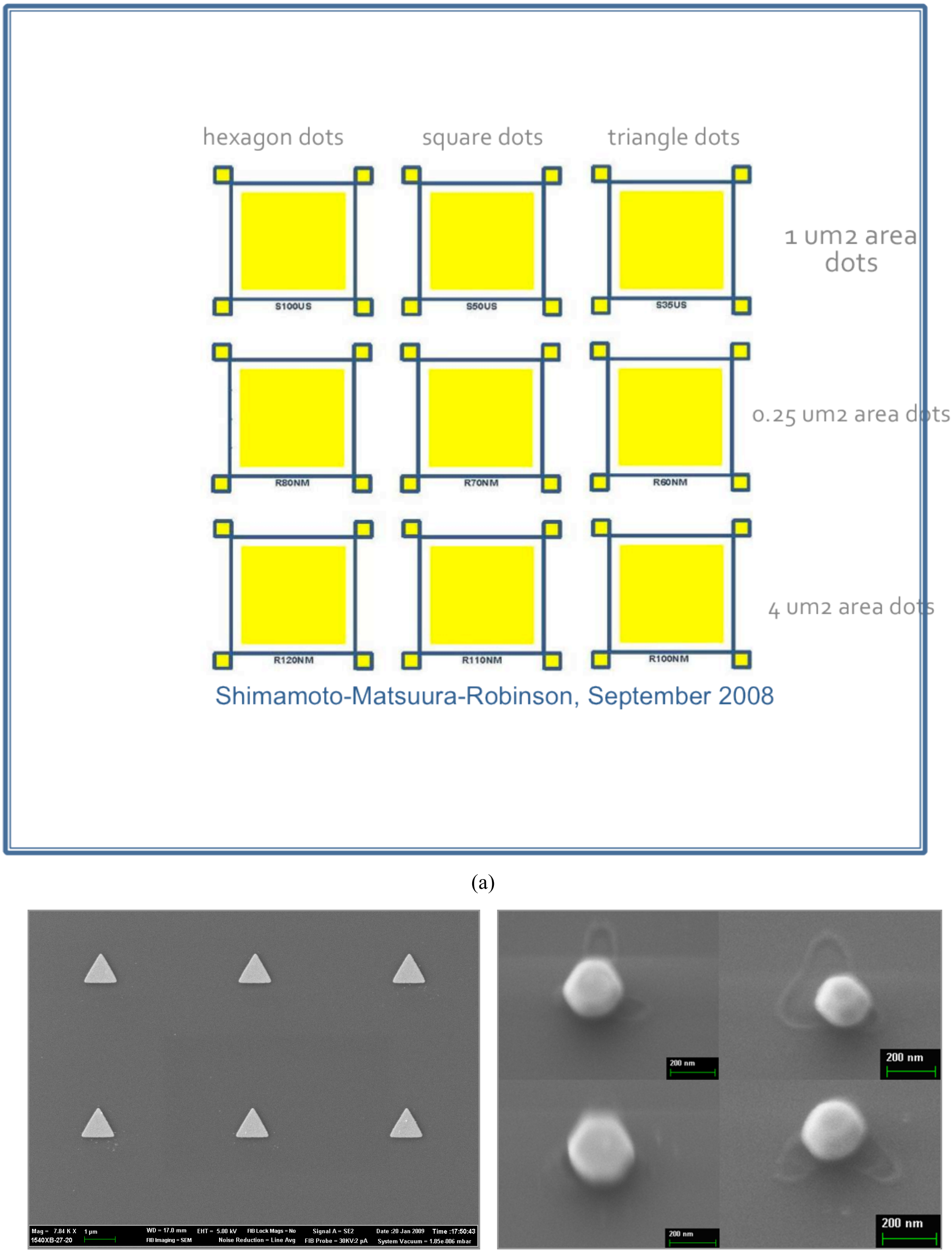

(a)

(b)

©

Figure 10. a) Diagram of first generation of patterned Au samples. b) SEM image close-up of some Au trigangular film dots prior to annealing, c) crystals after annealing.

Chapter 4 – Coherent X-ray Diffraction

The diffraction phenomenon can be seen all around us in nature. The dazzling spectrum of visible light in a rainbow, due to the wavelength dependent deviation of sunlight by tiny droplets of water in a cloud, is one such example. Diffraction occurs whenever a wave of any kind be it water, sound or light, encounters an obstacle. Its effects are most pronounced when a wave is incident upon a set of regularly spaced obstacles with separation distance comparable to the wavelength of the wave. In this chapter the fundamental aspects of x-ray diffraction will be explained and imaging methods utilising Coherent X-ray Diffraction (CXDI) will be discussed in some detail.

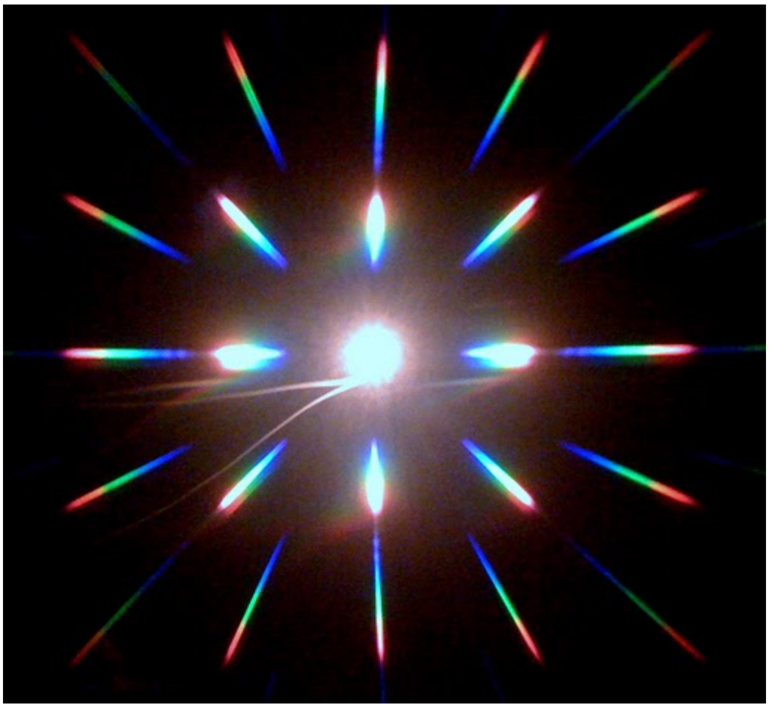

Figure 11. Diffraction from a common light bulb

X-ray Diffraction: revealing crystal structures

Since their first discovery by W. C Roentgen in 1895, x-rays have been instrumental in our investigations into the structure of matter. X-rays are simply a form of electromagnetic radiation with a shorter wavelength than that of visible light of around 1 Angstrom. This size range is of the same order of magnitude as an atomic spacing, making them ideal for use in the study of the structure of solids[13]. As a result of this short wavelength, x-rays also have very high energies making them ideal for penetrating solid materials. When x-rays are incident upon a material, some of these x-rays will be 'scattered' by the electrons in orbit of each atom. These properties have allowed x-rays to become one of the most useful tools in science. They have been used in the investigation of matter in numerous fields such as protein crystallography, materials science, medicine, astronomy archaeology and many others.

The experiments described later on in this report use highly coherent x-rays of 1.39Å (8.9KeV) produced at a third generation synchrotron source, such as the Advanced Photon Source, Argonne. These extremely bright, in-phase x-rays used in these experiments are utilised in order to probe the electron density of matter and study its 3D structure. They are highly penetrating, meaning they can probe deep into structures and they are also weakly interacting reducing multiple scattering problems.

Provided the kinematic approximation holds (each x-ray scatters elastically and only once), a plane wave of x-rays, incident upon an electron in an ordered series of atoms, will scatter producing a spherical wave from each point of electron density. These spherical waves then interfere with each other resulting in an interference pattern. Figure illustrates this interference effect for two planes of atoms with the same (h,k and l) miller indices which can be explained with Bragg's law[21]. If one atom is in a slightly different position due to a defect, there will be a different interatomic distance between it and its nearest neighbours. This will result in a phase difference between scattered x-rays from the out of place atom's electrons and those, which lie on the ideal lattice. This phase difference will show up in the interference pattern from the crystal and thus the interference pattern can, if measured sufficiently, reveal atomic displacements within a structure.

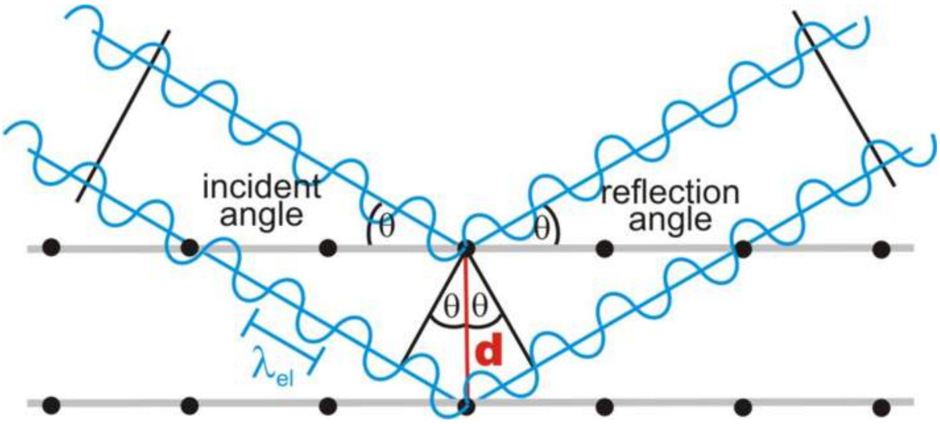

Figure 11. Diffraction of x-rays of λ wavelength by two parallel planes of atoms within a crystal.

Constructive interference of the two scattered waves will take place, provided the path length difference between scattered waves is a whole number of wavelengths, n. n is also the order of the reflection***[13]***.

$$n\lambda = 2d\sin\theta \qquad (12)$$

This equation is known as Bragg's law and describes the experimental conditions necessary for a constructive interference pattern to be observed on a detector. At every angle of 2θ where these constructive interference patterns can be seen, this is called a "Bragg peak'[22].

In reality, the coherence properties of x-rays used in typical CXDI experiments are not completely plane waves and have limited coherence properties. The spatial distance at which x-rays can be considered to be coherent defines longitudinal and transverse coherence properties [23]. The precise definition of coherence will be discussed in a later section.

The methods used in CXDI described, have been understood theoretically for many years. However, it was not until the advent of 3rd generation synchrotron sources that it became possible to develop this method experimentally. The CXDI method is totally reliant on our ability to produce highly coherent x-rays[24].

Coherent X-ray Diffraction Imaging (CXDI)

The goal in CXDI experiments in general is to try to reveal the remarkable and complex internal structure of a given sample. Very few methods allow the internal strain and density of a nanometre-sized crystal to be probed and subsequently analysed in such a way. It is a method, which can reveal a wide variety of physical properties in a sample, which may otherwise remain a mystery.

The light used in CXDI experiments is sometimes described as having 'laser like' properties, being both highly spatially and temporally correlated as opposed to the light emitted from your average laboratory x-ray source or light bulb. It had been possible to create coherent x-rays previously (reference), however it was not until the advent of 3rd generation synchrotron sources that x-rays of sufficient brilliance could be produced necessary to allow such a wide variety of experiments to take place[25, 26].

When a finite crystal is placed such that it is completely illuminated by the coherent part of an x-ray beam, then coherent x-ray diffraction is said to take place. Or, in other words, x-rays incident upon each electron in the scattering crystal will have the same relative phase with respect to the x-ray source. The scattered x-rays from such a sample will produce peaks in intensity on a sphere centred about the sample (the Ewald sphere) and at each reciprocal lattice point on this sphere there will lie a Bragg peak. Provided the full sample volume is enclosed by the coherent beam, then scattering from the entire extents of the crystal will interfere and produce a characteristic pattern of three dimensional (3D) intensity fringes about each Bragg peak[27] in the far field. This 3D diffraction pattern intensity can then be measured using an area CCD detector. Retrieval of structure information from such a diffraction pattern is then termed Coherent X-ray Diffraction Imaging.

The measured intensity $I(q)$ is related to the amplitude $A(q)$ by

$$I(q) = A(q)A^{*}(q) \tag{13}$$

$$A(q) = \int dr\rho(r)e^{-iq.r} \tag{14}$$

where $\rho(r)$ is the complex electron density function at a point r and $q = k_f - k_i$ is the momentum transfer between the incident k_i and scattered k_f waves[28, 29]. The direction of the Q vector is known and throughout the 3D rocking curve measurement is practically constant.

The recovered real space phase, ϕ describes any lattice distortions in the direction of Q vector, $Q = \phi.r$. The consequence of this is that one Bragg peak measurement only reveals one component of the displacement field and not the full strain tensor. It has been shown by Newton[29] that it is possible to measure the three non-coplanar Bragg reflections necessary to resolve the strain tensor. This will be discussed in depth in a later chapter, as well as further experimental procedures and results shown.

Experimentally, the intensity of scattered x-rays can be measured using a two dimensional (2D) Charge Coupled Device (CCD) detector which converts photon strikes into charge in order to be read out[30]. It is placed far enough away from the sample so that fine intensity fringes can be resolved. If we had a detector, which could measure both the reciprocal space amplitude and phase, then the electron density would directly follow by taking the inverse Fourier transform of the diffracted wave. Unfortunately, we only measure intensity of diffracted photons (the inverse Fourier transform of which gives us the autocorrelation function), so the phase information is lost. This problem is commonly known as the ‘phase problem’ and is encountered in many subjects such as x-ray crystallography and signal processing.

One solution to this phase problem is to sample the intensity signal finely enough to allow an algorithmic iterative approach to be used whereby certain known information (such as the known finite extents of the sample) is applied as a constraint in order to guess a possible set of phases. This will be discussed further in the next sections.

CXDI has proven to be an extremely useful tool in science and allows us to study the extraordinary properties of nanomaterials. Fourth generation x-ray free electron laser (XFEL) sources can now offer extremely high coherence properties and ultrashort, ultrafast pulses of x-ray light and ensure CXDI a bright future.

Oversampling

The solution to this version of the phase problem began with an extremely short letter by Sayre in 1952, detailing some implications to the measurement of electron density due to Shannon's theorem[31]. In order to solve the phase problem and allow inversion to direct space, it is necessary to oversample the diffraction pattern at greater than the Nyquist frequency[32, 33]. In other words our ability to determine a unique solution using an algorithmic approach depends on the sampling rate. The amount of oversampling is simply found by counting the number of pixels on the 2D detector per interference fringe. The critical Nyquist frequency of a the three dimensional phase problem is fully over determined if the complex amplitude is fully sampled i.e. sampled at each peak and trough[34]. The amplitude however, will be under sampled at this rate. Millane showed that in order to over sample the amplitude sufficiently, we actually require a different degree of oversampling in each dimension above 2. For a two dimensional problem, the oversampling rate must be 4 pixels per fringe; however if a third dimension is introduced, the critical sampling rate reduces to that of the amplitude critical frequency so for 2D x.y=2.2=4pixels per fringe and for 3D: x.y.z=2.2.1=4 pixels per fringe, oversampling is sufficient to uniquely describe the amplitude[35].

Coherence

Earlier, x-ray diffraction was discussed in terms of a perfect plane wave incident upon a sample. This is an ideal case and it is useful to examine some problems using a plane wave approximation; however, in CXDI, the precise coherence properties of the illuminating beam are crucial for producing the fringe or speckle patterns used to reveal the structure of a material. The development of 3rd generation synchrotron sources, some with coherence specific beamlines and recently 4th generation x-ray free electron lasers (XFELs) has allowed the CXDI technique to be possible due to their high coherence properties.

The degree of coherence of a beam is dependent on both the quality of the synchrotron source (undulator) and also the optical components employed in each experiment. A great deal of thought and experimentation goes into making each beamline at a synchrotron as efficient as is possible, in order to ensure the brightest and most finely tuned beam. The coherence of a beam is usually considered in terms of two components. These are the transverse (or temporal) coherence and longitudinal (or special) coherence and both are dependent on different beamline design parameters[22].

There are two quantities, which together make up a 3D region in space, which can be considered to be a coherent volume, which would enclose our sample of interest. These are the longitudinal coherence length and transverse coherence length.

Transverse Coherence

The transverse coherence is a beam property set by machine design and source properties. Transverse coherence ζ_T is dependent more specifically on the source size D and the distance from the source to the sample R and is itself divided into two components; the horizontal ζ_h and vertical ζ_v, thus providing the three dimensions necessary to give a coherence volume[36]. The values ζ_h and ζ_v are expected to be different due to the vertical and horizontal extents of the electron bunch when it reaches the undulator and the nature of its subsequent undulator induced oscillation. The meaning of the transverse coherence length is the separation distance inside the sample at which two points would see waves A and B (Please see figure 2 below) as being equivalent plane waves. These distances are defined as

$$\zeta_h = \frac{\lambda R}{(2\pi\sigma_h)} \text{ and } \quad \zeta_v = \frac{\lambda R}{(2\pi\sigma_v)} \tag{15}$$

where λ is the wavelength, σ_h is the horizontal source size and σ_v is the vertical source size.

Figure 2 shows the propagation of two plane waves A and B emitted from a source of size D. The point P is the point at which the waves are in phase with each other. The transverse coherence length is the distance from P we need to move, before the waves can be said to be out of phase with one another. At a distance of $2\zeta_h$, destructive interference will occur[37]. Often, focussing optics will be employed in order to increase the flux incident upon a particular sample. If this is the case then it follows that the alteration to the transverse coherence length will be the inverse of the magnification amount.

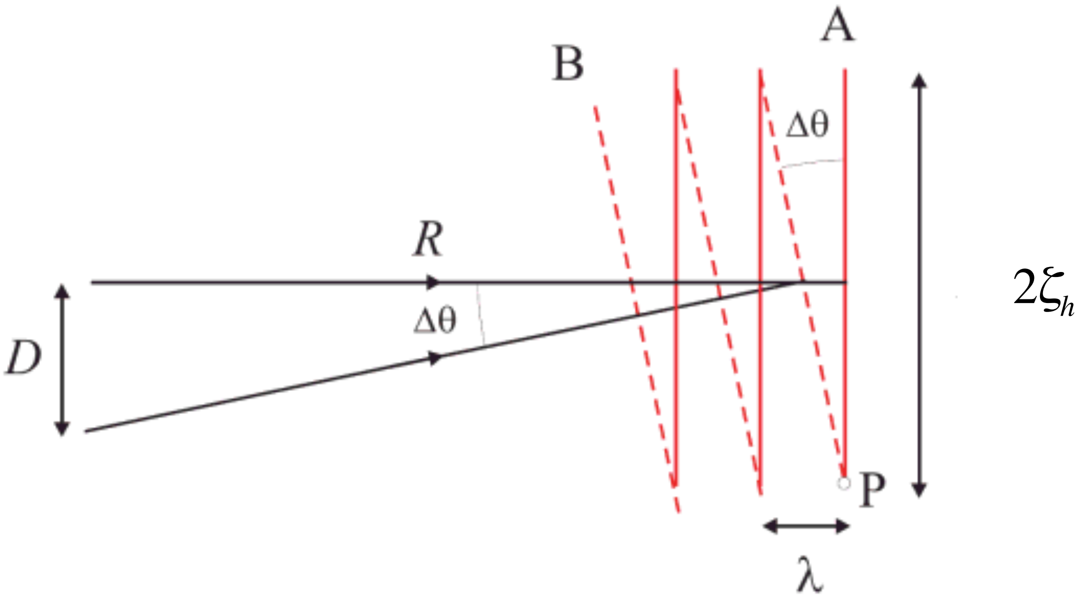

Figure 11 This shows two waves A and B of the same wavelength emitted from a source of size D, with distance R from source to sample and differing angles of propagation of $\Delta\theta$*. The point P is where the waves are in phase. Figure from reference [22].*

For a typical synchrotron source $\zeta_h = 10\mu m$ and $\zeta_v = 50\mu m$[36].

Longitudinal Coherence

The longitudinal coherence length ζ_L is bandwidth dependent as shown in figure 3. In this figure two waves of different wavelengths of λ and $\lambda - \Delta\lambda$ are shown propagating in the same direction. It is clear from the figure that the longitudinal coherence length is wavelength dependent. In experiments, which require extremely high coherence, a beamline optic called a monochromator is utilised (usually a Silicon crystal). The monochromator acts as a band pass filter, leaving a highly monochromatic, highly longitudinally coherent beam.

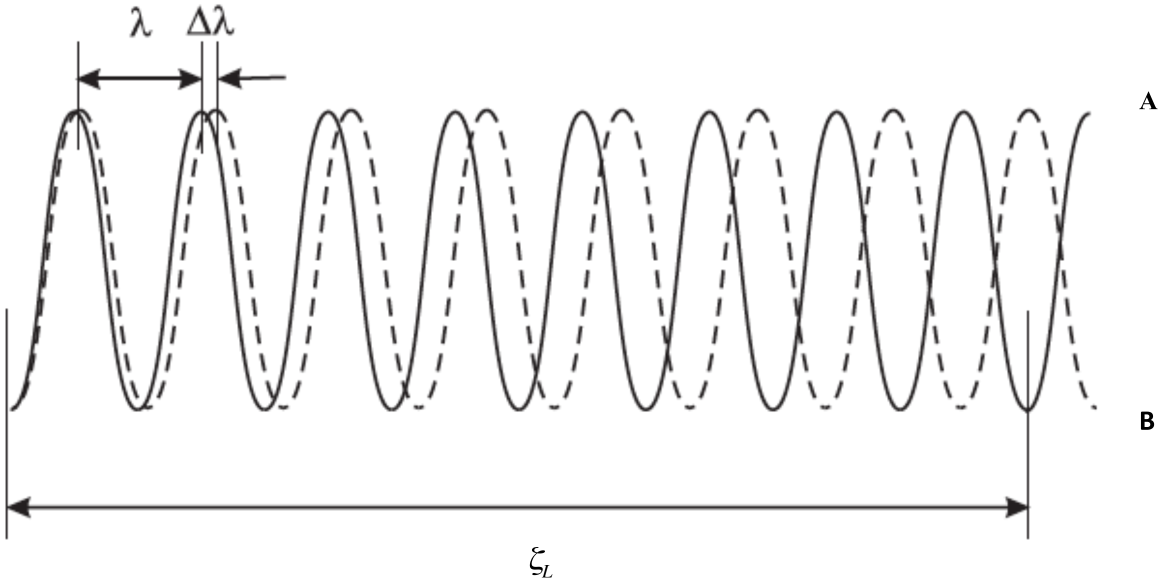

Figure 12 Shows two waves of different wavelengths emitted from the same source. The distance, ζ_L is the distance where the two lines (dashed and solid) become π out of phase from each other[25].

The longitudinal coherence length is defined as the distance ζ_L from two waves being in phase, to being out of phase. It follows that they will then be in phase again after travelling $2\zeta_L$. The longitudinal coherence can be expressed as

$$\zeta_L = \frac{\lambda^2}{2\Delta\lambda} \tag{16}$$

If the optical path length difference (OPLD) of all paths through the crystal under investigation is smaller than ζ_L, then the crystal is confined within the coherent part of the beam in the longitudinal direction.

Only when the extents of the sample are smaller than ζ_T and the optical path length difference through the crystal is smaller than ζ_L, can it be said that the crystal is coherently illuminated. Given that a typical source $\zeta_h = 10\mu m$ And $\zeta_v = 50\mu m$ and $\zeta_L = 0.8\mu m$, it can be said that the majority of the time, the limiting factor is the longitudinal coherence. This is the property of incident x-rays which can make or break an experiment. The OPLD is a distance dependent on the Bragg angle of the experiment, so depending on the dimensions of the sample under investigation, the incidence angle upon the sample can alter the degree of coherence of the experiment.

Phase Retrieval

The phase retrieval problem is an inverse problem encountered in many areas such as signal processing and optics. In CXDI, an x-ray intensity measurement is taken from a particular sample. Encoded in this recorded intensity pattern lies information on the electron density of the sample; however in order to reveal this information the lost phase of the complex amplitude must be recovered. As this lies in the reciprocal space world, the inverse Fourier transform (IFT) of this will provide us with a real space image of the object allowing us to better understand the sample in question[38].

In this section, an iterative, computational approach will be discussed whereby a guess is made of possible phase values, then the algorithm transforms data between real and reciprocal space applying constraints at each step. If a set of phase values are found which are consistent with measured data and constraints above a certain error metric, then a possible solution has been found. The IFT of the amplitude and phase values will then leave us with a real space image of the sample. Please see figure 12.

The algorithmic methods discussed are limited to phase recovery from objects, which are confined within a finite region in real space. The algorithms will be the Error reduction (ER) and Hybrid-Input-Output (HIO) by Fienup[39].

Sayre was the first to note that direct electron density structure determination would be possible given appropriate sampling of the diffraction pattern in 1952[31]. This idea was first implemented in the 1D by Vartanyants et al. when they studied x-ray reflectivity from Silicon surfaces with coherent x-rays in 1997[40]. The first 2D experiments were successfully attempted by Miao et al, where they looked at a set of Au nanocrystals. Robinson et al. were then able to reconstruct images of an Au nanocrystals shape [41] and realised the method’s potential at studying strain fields within crystalline structures. This demonstration by Robinson et al. used the HIO algorithm where the real space object is constrained to exist within a finite region in space. This is implemented using a box or so ‘support’ which the reconstructed object must be confined to.

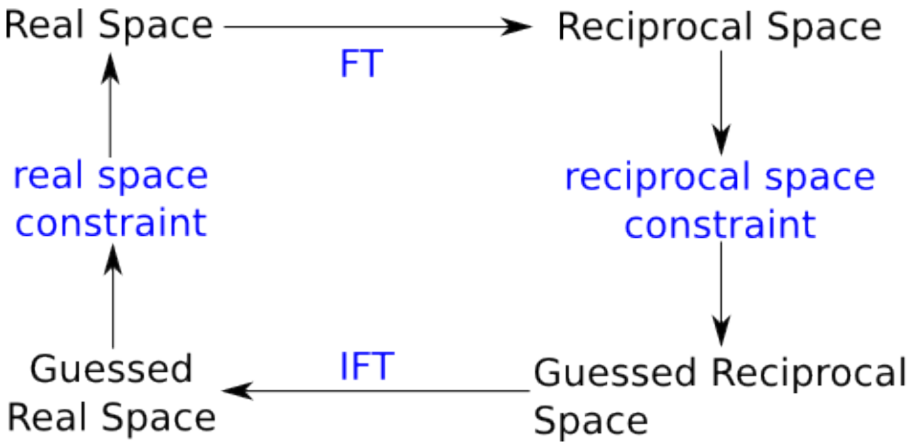

Figure 13 Diagram showing iterative process used in CXDI.

The experiments discussed in later sections involve CXDI in the Bragg geometry, where the diffraction pattern from a crystalline object is used to obtain real space images of the crystal. There are several advantages to the Bragg case as opposed to forward scattering, where a sample is placed in the beam and the transmitted x-rays are recorded on a detector. In Bragg geometry the sample and substrate are not required to be particularly transmissive. Secondly, the required rotation angle in the Bragg geometry to obtain a full 3D diffraction pattern, has been found to be only 1° rotation in theta (θ) as opposed to the 180° equivalent for transmission experiments, simplifying necessary sample alignment constraints massively[42, 43]. Lastly, no beamstop is required, meaning there is no lost intensity information. The most obvious drawback to using the Bragg geometry is that it is not possible to image non-crystalline objects, as they have no Bragg peaks. Additionally, in order to locate a Bragg peak from a given sample, it is necessary to align the crystal in the beam at the correct angles to put the Bragg peak squarely onto a finite detector area. As the precise crystallographic alignment of a sample is often unknown, this can prove to be extremely time consuming.

The iterative approach to the phase problem used in CXDI employs mathematical methods and attempts to recover phase information. The algorithms move back and forth between real and reciprocal space, applying constraints at each stage based on known information about our sample. Such constraints include positivity and the known size of our object. Some algorithms often utilised will now be discussed.

Error Reduction (ER)

The Error Reduction algorithm (ER) was developed by Fienup and is a modification of the Gerchberg Saxton (GS) algorithm. The GS algorithm was originally developed in order to recover phase information when intensity measurements have been made in both the real and the reciprocal domains[44]. There are two constraints applied in order to allow a result to be found and these are the measured amplitudes in real space and the measured amplitudes in reciprocal space. The workings of the GS algorithm can be described in four steps: 1) Make an estimate of the phase in the real space domain and Fourier transform it; 2) Replace the amplitude of the result with the measured amplitude; 3) Inverse Fourier transform the guessed phase and measured reciprocal space amplitude back to real space; 4) Replace the calculated amplitude of the object with the measured amplitude in real space[44].

The GS algorithm was modified by Fienup to allow a result to be obtained without the need for a real space measurement. The reciprocal space amplitude would still remain as a constraint; however the real space constraints were replaced with 1) Positivity: The real space amplitude must remain positive (which is to be expected); and 2) The real space object must be confined to within a finite volume in space (which is also to be expected). We know that when propagated back to the exit from the sample, our intensity pattern must have originated from a finite region in space; the sample. Where the amplitude point does not agree with both of these constraints, then the amplitude is set to zero[45].

The finite region constraint is applied with the use of a ‘support’, which is simply a shaped object, which the real space solution must exist within. This object can be any shape, but is usually a cuboid or ‘box support’, or a ‘shrinkwrap’ support where the support shape is itself iterated upon to get the closest possible fit. It has been found that the support size drastically increases the probability of convergence.

In this version, the ER algorithm works in the following way: 1) Start by using the chosen support as the estimate of the real space amplitude and combine with a guess of the real space phase, then Fourier transform this; 2) Replace the reciprocal space amplitude with the measured diffraction amplitudes; 3) Take the inverse Fourier transform of this to return to real space; 4) Apply the support constraint by setting all values which lie outside the support region to zero. Repeat the process until a solution is found which satisfies both constraints and also satisfies an error metric.

The particular error metric used, is found by simply comparing the measured data with the Fourier transform of the solution and provides a valid means of determining how accurate the solution is. This error metric is found by taking the normalised mean square error (nmse) between the reconstructed solution and the measured data [46].

$$E_{nmse}^{2} = \frac{\sum \left|A_{calc}\right|^{2} - \left|A_{meas}\right|^{2}}{\sum \left|A_{meas}\right|^{2}} \qquad (17)$$

where E_{nmse}^{2} is the normalised mean square error, A_{calc} is the reconstructed amplitude in reciprocal space and A_{meas} is the measured amplitude in reciprocal space. As E_{nmse}^{2} reaches 0, the solution becomes more accurate.

Using the ER algorithm, the error can either decrease between successive iterations or stay the same. The algorithm tends to converge upon a solution rapidly for the first few iterations, but then it slows down considerably. This is because once all of the calculated amplitudes are confined within the support, the algorithm will stagnate[37].

A modification to the ER algorithm has been made by Ross Harder dubbed PO-ER (Phase only ER)[47]. This altered version of ER has slightly different constraints in real space, as it allows amplitude to exist outside the support region, provided the phase is zero.

Hybrid Input Output – HIO

The motivation behind creating HIO was primarily the slow convergence of the ER algorithm and because of 'stagnation' in local minima[44]. The algorithm is identical to ER apart from the fact that the constraints are different. The algorithm still begins in real space with a first guess, Fourier transforms this, applies reciprocal space constraints, then inverse Fourier transforms this to real space. The difference with this algorithm is that the resulting real space result is no longer simply a possible solution, but it becomes a driving force for the next iteration. In other words, the starting point (a combination of the previous iteration and current iteration) leads to the output. The advantage of this being that any output will automatically be consistent with the reciprocal space constraints, so any result which is also consistent with the real space constraints is a solution.

$$g_{k+1}(x) = \begin{cases} g_k(x), & x \notin \gamma \\ g_k(x) - \beta g'_k(x), & x \in \gamma \end{cases} \tag{18}$$

where $g_k(x)$ is the current iterate, β is a constant which determines how much of the previous iterate will be included in the next (usually use a value of β=0.9 is used), and γ is a set of values where $g_k(x)$ violates the constraints.

Several modifications to HIO have been made, one of which is Phase Constrained HIO (PC-HIO). This algorithm simply includes an additional constraint that all phases in real space must be confined to within a certain range of values (as opposed to the full range between 0 and 2π). This can be an advantage for crystals, which are likely to have small variations in phase range.

Guided HIO or gHIO is another modification to the HIO algorithm whereby many successive solutions are combined in the hopes of improving the final result. First developed by Miao et al[48]. The concept is that the results from a number of independent HIO iterations are averaged together. This average then acts as a starting point or seed for future iterations. The process is repeated until a solution is found which is fitting with HIO constraints and an error metric. Phasing can sometimes produce differing solutions, which tally with constraints and the error metric making the true result ambiguous. gHIO attempts to improve upon the result by averaging out these multiple solutions. Multiple solutions can then also be averaged together to provide a more realistic solution.

Shrinkwrap vs. Box Supports

The support defines the region in space in which solutions are constrained to reside within. In the 3D case, the support is defined as a set of planes in three dimensions, which enclose a volume. As discussed previously there are a number of ways in which a suitable support can be chosen with which a solution can be found (with ER and HIO algorithms and variants). Two support types are the box support and shrinkwrapped support. The support can make a vast amount of difference to the outcome of phasing operations, so picking a support is crucial. Due to the large number of variables at play (data preparation, algorithm settings, support picking etc.), phasing can sometimes be a very time-consuming task, especially since it is not always clear which variable needs altering to obtain a more accurate result.

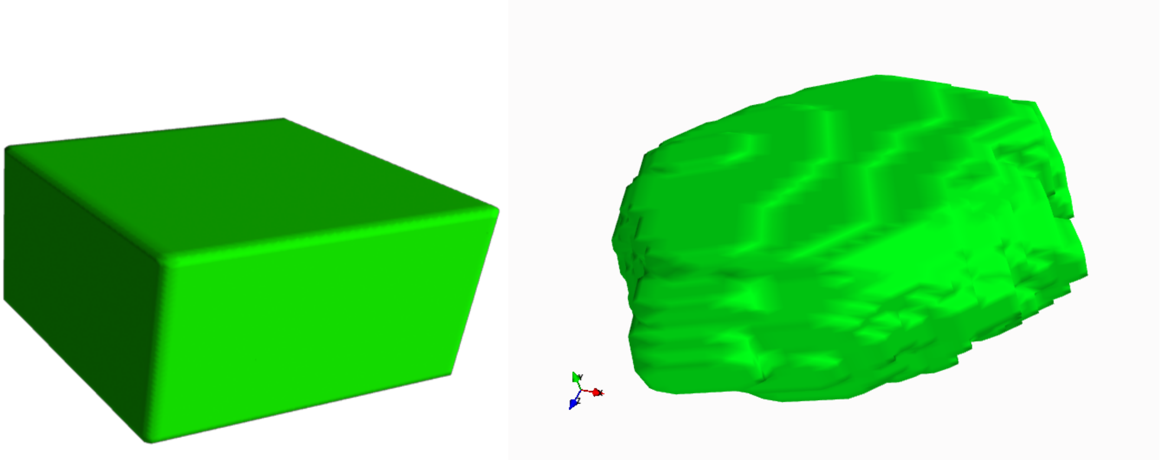

Figure 14 typical 'box support' (left) and shrinkwrap support (right)

A custom version of the shrinkwrap support, originally developed by Marchesini et al[49], was created by MC Newton at UCL and has been successfully used to reconstruct images from ZnO nanorods[29]. This version has been tested and used extensively to obtain some of the results discussed in later sections. It has shown to improve results when compared with a similar box support. In this form the measured intensity $I(q)$, is Fourier transformed to give the autocorrelation function, $p(-r)^* p(r)$. A 2D cut through the centre of the brightest voxel of the autocorrelation function is then taken. The plane on which this slice is taken (in x,y,z) is defined by the user according to the expected shape of the crystal. It was found that if the sample has any prominent parallel facets, the result is improved by aligning the plan to these facets. Next, a user-defined threshold is applied to the slice. The thresholded 2D autocorrelation slice or 'seed slice' is then overlaid along the entire length of the autocorrelation function in a direction perpendicular to the chosen seed slice plane at the brightest voxel in each plane. The resulting object is then convolved with a moving average (to smooth the result) and Gaussian function (to ensure support larger than reconstructed object). This provides us with an initial 'shrinkwrap' support with a much more similar shape to our reconstructed object than a typical box support. Phasing using this support to constrain iterations can then commence. Figure 13 shows the shape of a typical shrinkwrap support object, compared with a similar box support.

During phasing, the support will be further refined as the algorithm converges upon a solution. Starting from the initial support, 100 iterations of PC-HIO are carried out followed by 5 iterations of ER. At this point, a 20% threshold (set by the variable ‘Array2SupportThreshold’ in phasing programs) of the reconstructed object shape is convolved with the initial support, a moving average and a Gaussian function in order to create an updated support[29]. Then 40 PC-HIO followed by 5 ER iterations are carried out before a new support is calculated by the same process discussed previously. A convergence threshold is applied at each support refinement step, until the desired result is achieved consistent with support threshold, algorithm constraints and error metric values.

Displacement Field

Provided a solution is found using the iterative algorithmic approach, we can then analyse the recovered phase information in order to interpret strain fields within the crystal of interest and better understand the physical world on the nanoscale. Ions displaced from their ideal lattice positions will result in a phase shift in ϕ (recovered real space phase) in the direction of $Q = \phi.r$, meaning that one set of recovered phases from one Bragg reflection only provides one component of the displacement field. Thus we do not have a full description of 3D displacement information from within the crystal. Subsequently, one reconstruction may not be sensitive to certain defects and distortions due to their crystallographic alignment, which may actually exist and yet are not visible through a single reconstruction.

Although much can be learnt from a reconstructed real space image from one Bragg peak, a fuller picture can be seen with the addition of two or more further measurements when we can calculate the displacement field (D-field). The problem is over determined for every value of non-coplanar Bragg reflections where the number of measurements n > 3, but when n = 3, we can invert to find the solution exactly[29, 50].

It is worth noting that the ability to experimentally measure multiple Bragg peaks is not useful for the sole purpose of constructing D-fields. By comparing reconstructions from different Bragg peaks, the resulting dimensions, shape, nature of defects, nature of displacements, validity of reconstructions etc. can be compared.

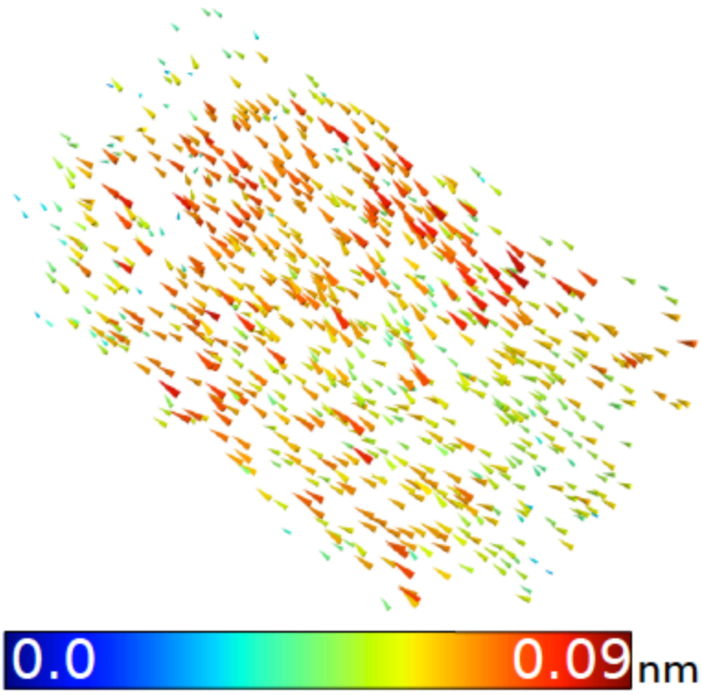

Figure 15 3D representation of a D-field reconstructed from multiple Bragg peaks from a ZnO crystal. The direction of arrows shows the direction of displacement and the colour and size represent their magnitude. Image modified from Newton et al. [29]

The scripts used in D-field calculation later in this report are modified versions of those first developed by Marcus Newton.

Measurement of multiple Bragg peaks is not entirely a trivial task. It was successfully achieved for the first time at the Advanced Photon Source (APS) beamline 34-ID-C using a confocal alignment microscope to measure 6 Bragg peaks from the same 200nm Au crystal. The methods employed will be discussed in detail in a later section. These datasets were then successfully reconstructed and used to create a D-Field.

In order to do this, the reconstructed real space images from each Bragg peak must first be de-twinned to allow alignment. ‘Twinning’ or enantiomorphs are an inherent problem in phase retrieval from diffraction patterns. Provided that the support constraint applied during iterative phase retrieval is symmetric, there is 50% chance of obtaining a real space solution, which is the complex conjugate of the ‘actual solution’. The actual solution can only be known with a priori information about the sample shape and alignment relative to the substrate given the experimental geometry. In other words, crystals are often asymmetric in a predictable way due to the interactions with the substrate. This allows twins to be identified.

Once de-twinned, the multiple reflections need to be aligned with one another. This is because reconstructions will lie in the laboratory reference frame and not sample reference frame, thus a simple geometric rotation is carried out based upon known experimental geometry and detector angles. The final step is then to align the reconstructions in x, y, z by eye in 3D visualisation software (such as MayaVi).

As the reconstructions do not share the same coordinate systems at this point, reconstructions are then interpolated onto a cubic grid system (at a user defined interval for example 25nm) in order to construct the D-Field.

Chapter 5 - Experiments and Reconstructions

This section will outline the basic experimental procedure used in all CXDI experiments carried out in this research. It will first describe the basic experimental setup used to measure Bragg peaks at beamline 34-ID-C of the Advanced Photon Source (APS) in Chicago, then go on to discuss specific experiments undertaken and results from these experiments. These experiments will demonstrate applications of CXDI to study Laser heating in Au, Laser shock damage in metals using X-ray Pump Probe (XPP) techniques, FIB damage, investigations of crystal 'twinning', spontaneous planar defects and finally, using the method of multiple Bragg peak CXDI to visualise strain in a single Au crystal by constructing a Displacement Field (D-Field).

Basic Experiment Procedure

In order to study the wonderful array of properties, which nano-crystalline materials can exhibit, we use the method of Coherent X-ray Diffraction Imaging (CXDI). Experiments have been done at beamline 34-ID-C of the APS. This beamline is an Insertion Device (ID) beamline and employs finely engineered optics and other highly advanced equipment in order to create an x-ray beam with a large coherence volume, vital to allow these experiments. X-rays from a U33 undulator in vacuum are monochromatized by a Si (111) monochromator (46m from source) with an energy E = 9KeV ($\lambda = 0.139$m). The x-rays are focussed with a set of Kirkpatrick-Baez (KB) mirrors to a spot size of 1μm^2 onto the sample, giving an increased flux and therefore increased effective resolution in images (51m), which sits on an accurate XYZ goniometer stage.

The basic experiment simply involves placing a crystal of interest into the beam at the appropriate positions and angles such that a Bragg peak can be measured. The sample is illuminated so that diffraction from every part of the crystal takes place (the entire crystal is enclosed in the coherent part of the beam). The interaction of these diffracted rays produces a characteristic diffraction pattern, which has been measured in the far field on a two dimensional (2D) pixel area detector with 1242x1154 pixels of 22.5µm size. The detector is placed far enough away, that fringes resulting from its finite size can be fully resolved. In order to measure a three dimensional (3D) diffraction pattern with a 2D detector, the sample stage is rotated in steps of 0.02° in theta (θ) with a new detector measurement at each new position. These separate slices are then stacked together to produce an almost parallel series of 2D cuts through the 3D diffraction pattern. Rotation of the sample in this manner is equivalent to moving the CXD pattern through the detector, nearly perpendicular to the detector plane.

Samples used often consist of a substrate on which millions of crystals have been prepared. The unfortunate consequence of the sizes and sheer number of crystals involved is that it is extremely difficult to determine after the fact, which crystal on a given sample has actually been measured. The comparison with 'real world' images of the same crystal is obviously quite useful for a number of reasons. It would firstly allow any reconstructions (achieved with phasing methods detailed earlier on) to be compared with microscope images such as Scanning Electron Microscope (SEM) images, allowing direct verification of results. It also opens up the door to all manner of interesting experiments whereby a crystal is measured, then removed and damaged or altered in some way, then measured again at a later date in order to understand the effects of the introduced changes.

We have successfully demonstrated how this can be achieved by using a set of patterned samples used in conjunction with an in-situ confocal microscope placed at the beamline. This allows the exact crystal being measured to be determined while measurement is under way and in turn enables the crystal to be viewed with SEM measurements at a later date, then returned to after changes have been introduced to the sample. The specific procedure used to do this will be discussed in the next sections.

Confocal Microscope Alignment Method: measuring crystals multiple times[30]

In order to measure a crystal multiple times and also measure multiple Bragg reflections from a single 200nm crystal, it is first necessary to determine the diffractometer centre of rotation. The sample stage angles phi and chi (pitch and roll) are set such that the sample is flat. The confocal microscope (in camera mode) is then used to locate a feature on the sample, which is observed as the sample is rotated to -180º, -90º, 0º and 90º in theta (yaw). The intersection of these four new positions gives an accurate (to 2 μm) centre of rotation. The next stage is to align the highly focussed x-ray beam so that it passes through this centre of rotation. The sample is replaced with a phosphor screen, which converts the x-ray beam into visible light. This is placed on the diffractometer and brought into focus by varying the confocal microscope height. This confocal height is then used as a height reference point for the remainder of the experiment. So that visible light from the phosphor screen can be seen, the confocal microscope is set in "camera mode", where the confocal microscope acts as a regular light microscope. The sample height (z) is then varied until the x-ray beam is seen to shift into the previously determined centre of rotation (see Fig. 1a). Alignment of the x-ray beam with the known centre of rotation is further refined by varying the horizontal translation positions of a set of KB focusing optics. This alignment procedure has been found to provide positioning of the beam with 1 μm accuracy.

The sample is returned to the diffractometer stage and sample height (z) is varied until the sample is in focus under the confocal microscope. This also brings the sample into the focal point of the x-ray beam. Fine-tuning of the vertical sample positioning is achieved using the microscope in confocal mode. In this setting, the microscope is extremely sensitive to focus in the z direction, especially when the sample is tilted (see Fig. 2c). As can be seen there is only a narrow band of sample in focus and an equally small x-ray footprint. The combination of beam alignment with diffractometer centre of rotation and high accuracy vertical positioning of the confocal microscope is highly useful. It allows a Bragg reflection to be measured from a particular 200nm crystal and its corresponding reconstruction to be compared with real-world SEM images of the same nanocrystal.

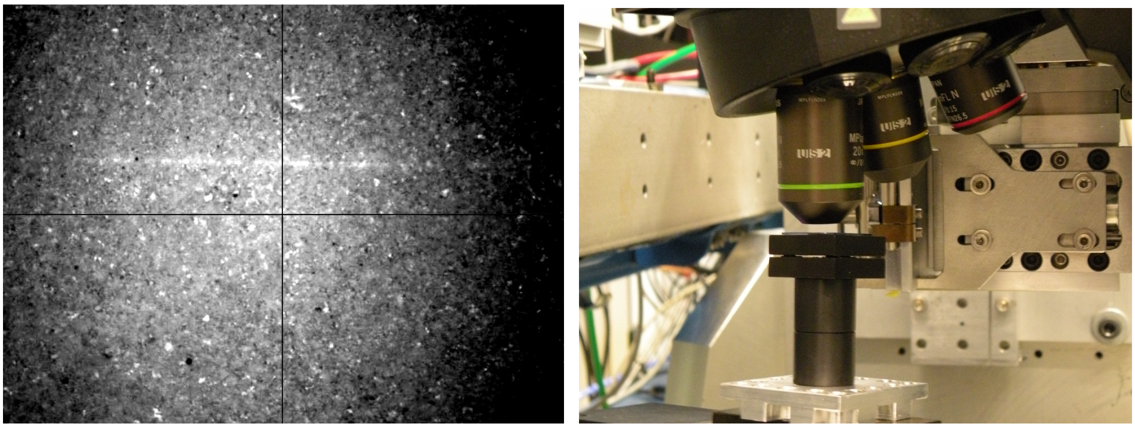

(a) (b)

Figure 16. *(a) X-ray beam footprint on phosphor screen viewed through confocal microscope in "camera mode". (b) Confocal microscope in-situ on diffractometer at beamline 34-ID-C, Advanced Photon Source.*

A set of samples have been produced using e-beam lithography which consist of an array of thousands of Au film 'dots' on a silicon substrate. When high temperature annealed, these film patches form individual nanocrystals whose size is dependent on the size of initial film deposit. A 0.25 μm^2 area film 'dot' will routinely form a single 200nm crystal ideal for CXD (see Fig. 2d). In order to measure multiple Bragg peaks from the same 200nm Au crystal it is first necessary to carry out the beam alignment described earlier. Due to the small size of the crystals, a 20x objective lens and a software magnification of 2x was used.

Finding a Bragg peak

The sample is placed on the diffractometer and tilted to ensure a small beam footprint (8° angle of incidence). It is assumed that when the Au crystals are annealed, they form oriented with 111 pointing up, perpendicular to the substrate. This possible reflection is entered into beamline control software (SPEC), which then calculates the approximate motor positions to place another Bragg reflection on the CCD detector. The crystal of interest is brought into the x-ray beam focal point and rotated about theta in small steps (yaw) until a Bragg peak is located on the CCD detector. The centre (brightest slice) of the Bragg reflection is then found by refining stage translation motor positions (x, y, z) and angle motor positions (phi, chi, theta). Then a full 3D Bragg reflection is measured by recording 2D images of the Bragg peak intensity as the sample is rotated in theta in steps of 0.02º. These slices are then stacked together to form a 'z-stack' of the Bragg reflection. Once found, the precise motor positions of the reflection are entered into SPEC and further Bragg reflection motor positions can be calculated with increased accuracy. These other sets of motor positions for each Bragg reflection are then moved to. The brightest slice of the peak is found once again and another set of 2D images of this second reflection are recorded. This process of locating and recording multiple Bragg reflections is now routinely used to locate 6 reflections (or more) from the same 200nm Au crystal and is highly time efficient. Evidence that multiple reflections recorded are from the same nanocrystal, can be seen in Fig. 2d where burn marks are visible on the silicon substrate due to the measurement of 6 reflections.

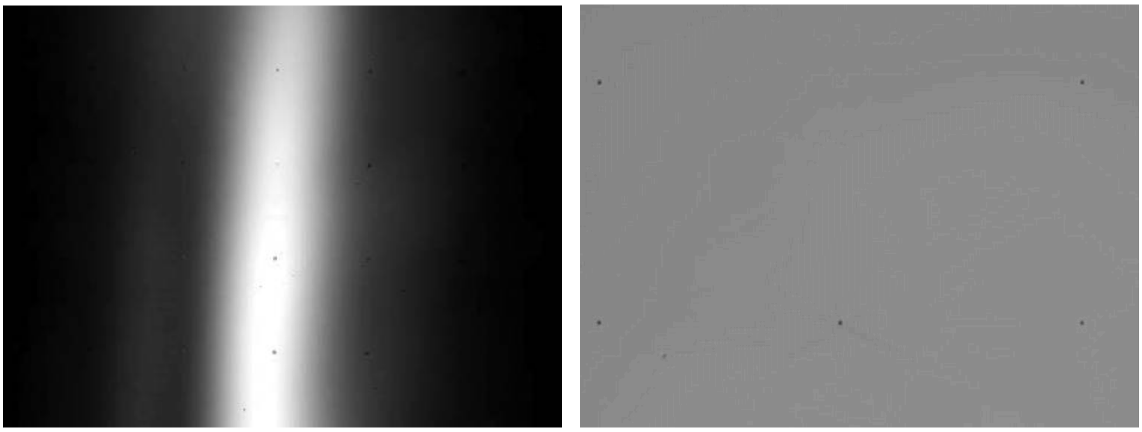

(c) (d)

Figure 17. *(c) Confocal image of highly tilted sample under confocal microscope. (d) Confocal image of Au nanocrystal array with x-ray burn marks due to multiple Bragg reflection measurement.*

Measurement Settings

Once the Bragg peak we wish to measure has been located on the detector it, is then a simple case of 'peaking it up'. This involves finely altering various diffractometer angles and sample stage positions until the Bragg peak produces the brightest image on our detector. The positions altered in order to do this are the horizontal sample translation motors (x and y), the vertical sample height (z) and the sample angle (θ).

Then a region of interest (ROI) is set which is simply a user-defined area on the 2D detector, which is to be read out. This is determined according to the shape of the diffraction pattern on the detector. The reason for doing this is that readout time is one of the largest barriers in obtaining good measurements. The sample will shift out of alignment after an hour or two so it is vital to increase the time efficiency of measurements in order to ensure good statistics. The quicker a frame can be recorded, the more measurements can be taken in our allotted 1-2 hour window before we lose alignment.

In order to avoid detector saturation when measuring a very bright pattern, a shutter is placed in the beam path as data is being read from the detector. If a Bragg peak is exceptionally bright, we sometimes need to introduce attenuation into the beam to reduce the risk of detector saturation, which can damage the detector. Attenuation is introduced as sheets of Mo film and Al film of various thicknesses.

One of the key concerns during measurement is that the oversampling ratio is maintained in order to allow phase recovery to be possible. This must be done in all three dimensions including the x and y dimensions on the CCD detector, but also in the stacking dimension (determined by rotation of the sample stage, θ). In order to ensure the measurements are sufficiently oversampled, the rotation steps used in theta must be checked carefully by the user.

Effects of Laser induced heating of Au crystals

Revealing the 3D structure of highly strained nanoscrystals under extreme conditions is an important step in explaining their unusual physical properties and understanding some of their new and emerging applications to science and technology[29, 38]. Many dynamical processes, which can be seen occurring in nanomaterials, can be drastically different to the behaviour seen in the bulk case[51, 52].

In order to study some of these processes, our group carried out two experiments at beamlines 34-ID-C and 7-ID-C of the APS light source. The overall goal of these experiments was to build up a detailed picture of the lattice response in gold nanocrystals upon rapid heating and cooling. The response was being studied as a function of incident laser power and laser/x-ray bunch timing offset in a pump probe experiment. This research has enormously important implications in explaining the behaviour of nanomaterials under extreme conditions induced by a laser.

One such question the research hoped to answer was how the generation of planar defects in nanocrystals would be dependent on particle size. A high density of dislocations are expected as a result of laser shock compression, which may be observed in reconstructed 3D images of crystalline lattice deformation.

The two experiments carried out were 1) Au crystals were measured with CXDI before and after damage was caused by a high power laser ex-situ; 2) an X-ray Pump Probe (XPP) experiment where Au crystals simultaneously imaged with coherent x-rays and illuminated with a femtosecond 88 MHz Ti: Sapphire laser. The results from the second experiment are still in preparation so only results from 1 will be discussed.

Experimental Method

A set of patterned Au nanocrystals on an SiO2 substrate were used in this experiment. The sample was placed on a ‘kinematic’ mount, which is a magnetic sample mount allowing the sample to be removed and accurately placed back in exactly the same position. The detector was moved to the angles necessary to record a $11\bar{1}$ Bragg reflection from gold. Using the confocal alignment methods detailed in an earlier section, the crystal of interest was brought into the known beam location. Next, the sample was placed at a high incidence angle of $\alpha = 8°$ and rotated in θ until the $11\bar{1}$ was found on the CCD detector. Then several datasets were recorded to allow real space images of the amplitude and phase to be constructed. The sample was then removed from the diffractometer in order to be irradiated with an ex-situ laser.

The sample was irradiated with an Nd: YAG laser at 248 nm with 24 ns pulses. After irradiation, the sample was then returned to the diffractometer at the beamline in order to measure another 3D diffraction pattern. Then it would be removed again and irradiated again at a higher dose. The doses were 0, 0.0134 J/cm^2, 0.026 J/cm^2 and 0.026 J/cm^2 x10 (irradiated 10 times at the same power level). After the last irradiation iteration, the damage to the sample was obvious and could be seen with the naked eye. Sections of Au nanocrystals which were previously visible had been blasted from the face of the sample.

Results

After datasets were recorded, the process of reconstructing images began. The images in this section show the results from several reconstructions as well as some of the datasets used to construct them. Figure 17 and 18 each show a series of 2D slices through the 3D Bragg peak intensity pattern. In order to create the images, a background measurement was subtracted in order to remove any unwanted noise; then, aliens were deleted (several cosmic rays at the edges of the detector). The data are shown on a logarithmic scale due to the large dynamic range of the measurements. As can be seen in these figures, there are several differences between the Bragg peaks before and after laser irradiation. Before the peak is much brighter in intensity with the brightest pixel recording 303.63 photon counts in a single 0.1s exposure (45500.46 per exposure and one photon gives 140-150 ADU's therefore 45500.46/150=303.64). After the laser damage, the brightest pixel read half of this amount at 135.58 pixels per exposure. Another difference is that the after measurement seems to be missing certain features. On the bottom left and top right of the Bragg peak centre, fringes previously visible have all but disappeared.

The diffraction patterns measured were reconstructed in order to recover the lost phase information and produce images of real space amplitude and phase. A background dataset was subtracted from the data to reduce the effects of noise in the data. Any cosmic rays were removed (provided they were not interfering with fringes. The data were binned with 2x2 binning in order to reduce computational time ensuring oversampling was maintained. Then phasing could be done. A threshold of 400 was applied to the intensity and the phase was constrained throughout computation to remain within $\pm\pi/2$. Shrinkwrap was used in order to create a tighter support and an example of a typical support can be seen in figure 20b. 200 iterations of pc-HIO were done followed by 10 ER iterations, then the shrinkwrap support was reformed followed by cycles of 10 pc-HIO, 2 ER iterations, support recalculation, 10 pc-HIO, 2 ER, support recalculation and so on until a solution was found.

Figure 19 shows the reconstructed complex amplitude (density) of the irradiated crystal prior to irradiation, after the lower dose and after 10 pulses of the higher dose. Figure 20b shows an SEM image taken soon after the experiment of the same crystal measured. There is quite good resemblance especially with Figure 19d in the shape of the crystal.

As can be seen in all three dose levels, there is a missing slab of amplitude in the centre of the crystal perpendicular to the vertical axis. This is quite clearly not real, so why does there appear to be a gap in the reconstructions? The answer is likely that there is a twin crystal in the gap with a different crystallographic. It could be a section of reverse stacking which we are not sensitive to due to the direction of the Q-vector in these measurements. By returning to the crystal and measuring multiple Bragg reflections, it is likely that the missing piece would appear filled in, in some other Bragg reflection measurements.

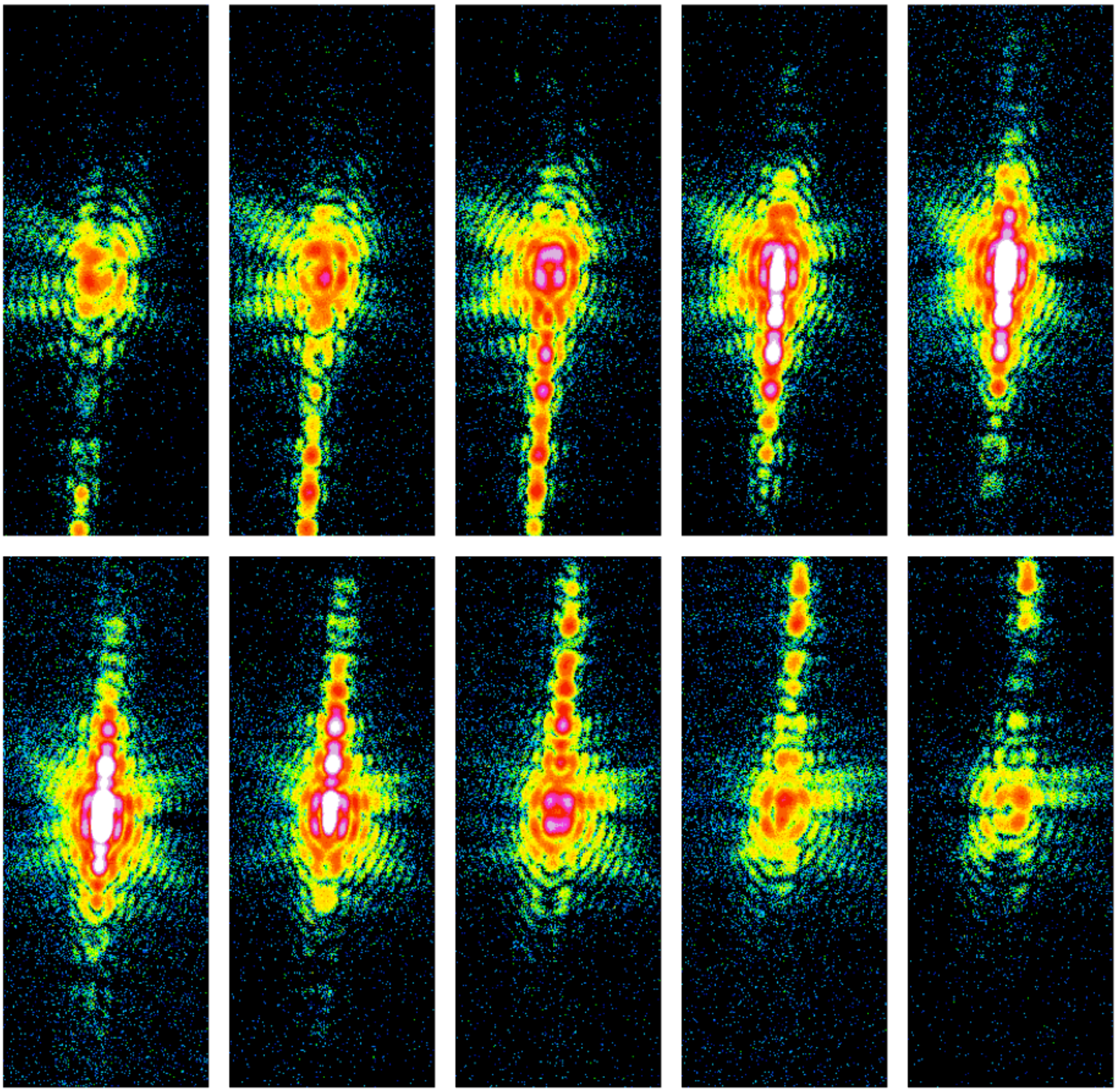

Figure 18. *A selection of 2D slices of intensity measurements from the Bragg peak of a 200nm Au crystal (dataset 56-74) recorded prior to laser irradiation.*

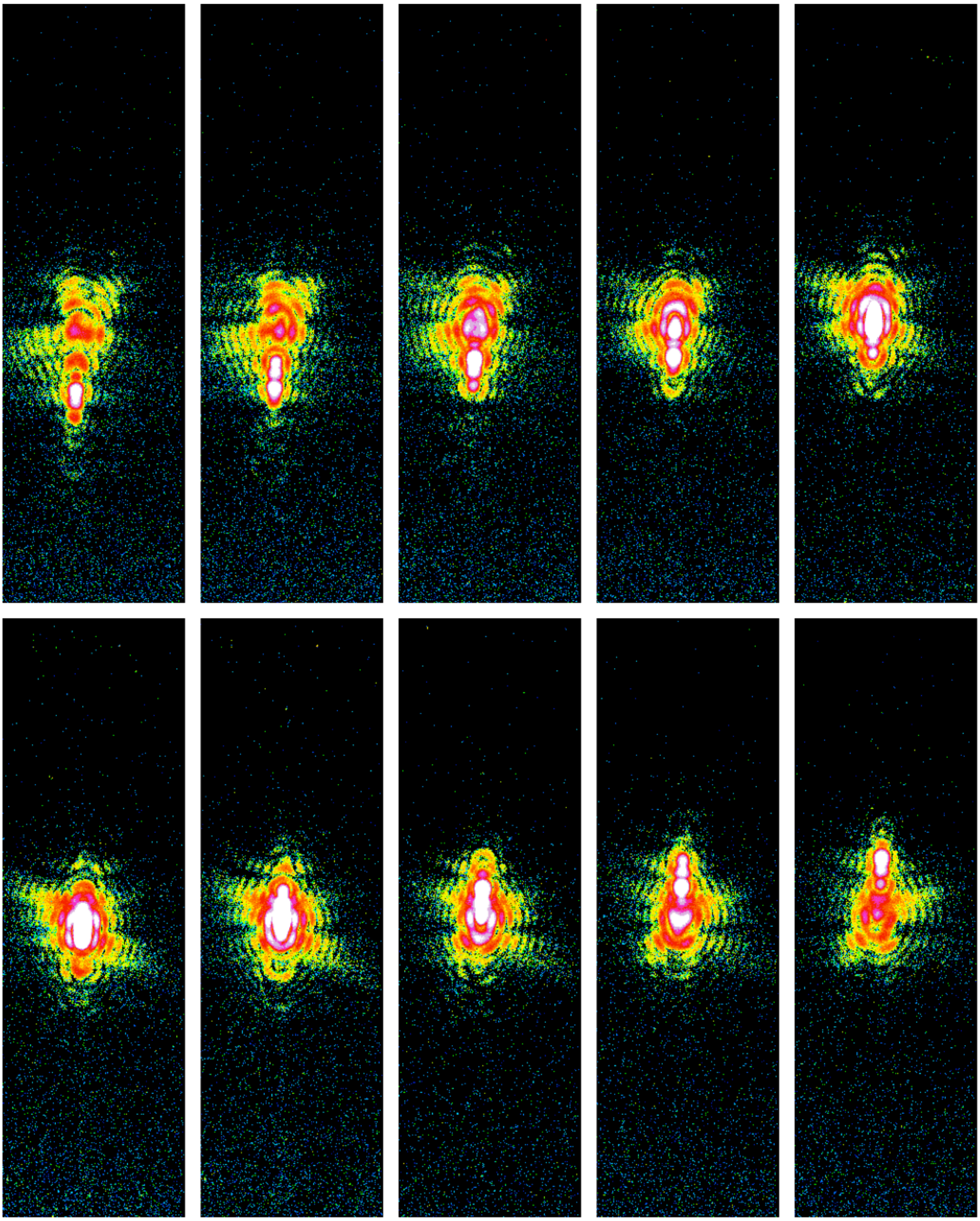

Figure 19. *A selection of 2D slices of intensity measurements from the Bragg peak of a 200nm Au crystal (dataset 56-74) recorded after irradiation at the maximum laser power (0.026* J/cm^2 *x10 pulses)*

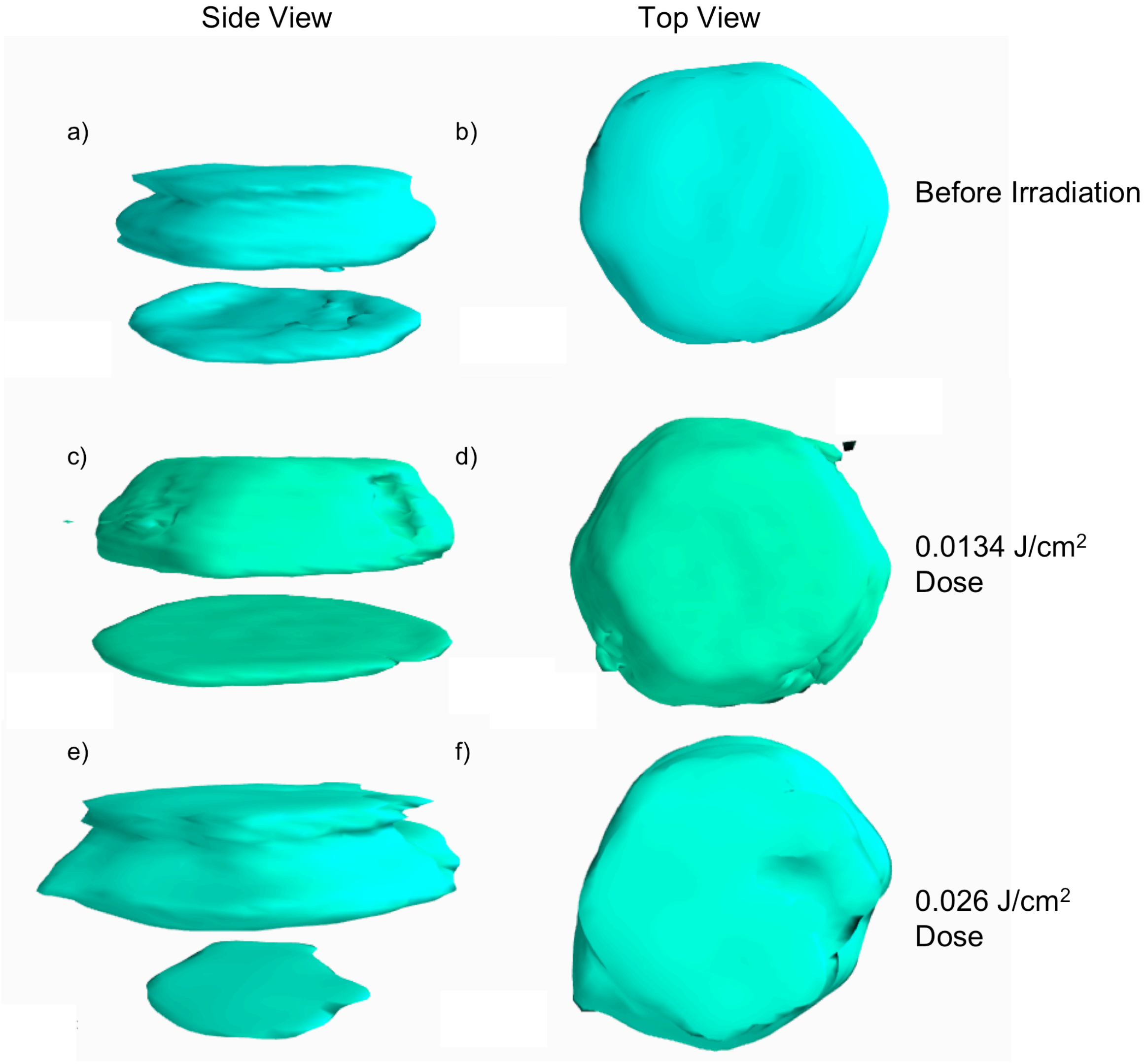

Figure 20. *a-f) Reconstructed complex amplitude (density) of crystal before and after different levels of irradiation.*

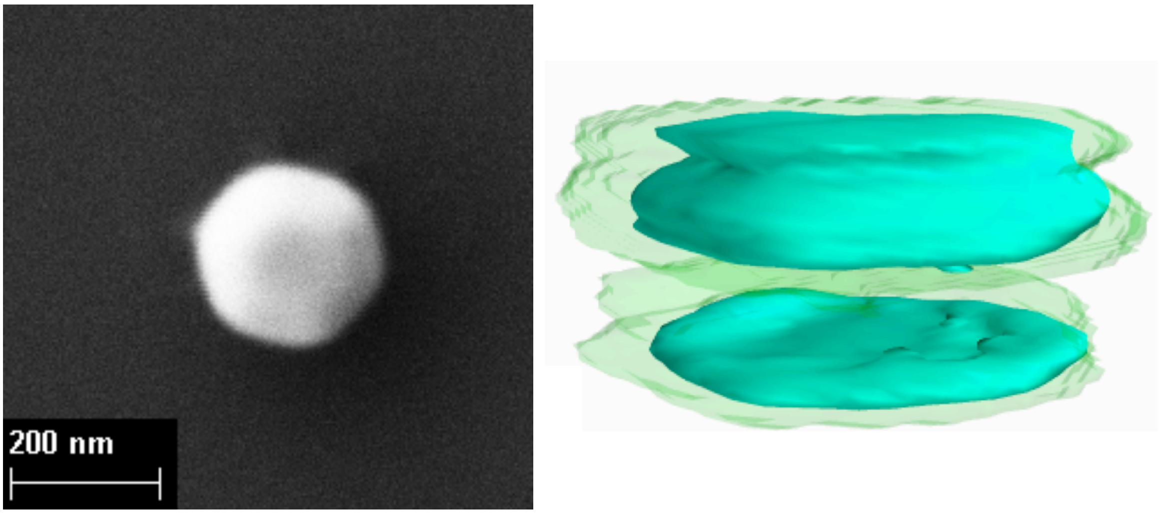

Figure 21. *Left) Scanning electron micrograph image of the irradiated crystal. Right) shrinkwrap support (translucent) wrapped around reconstructed complex amplitude from Au crystal.*

The missing piece seen in the reconstructions is what causes the very interesting twin fringes seen in figures 17 and 18. It is clear in both figures, that the diffraction patterns are very interesting in nature. For one thing, there appear to be double fringes in the vertical fringes. This characteristic of twinned peaks is indicative of a crystal with two distinct pieces of the crystal with a phase offset from one another. As a result of the phase offset, the diffracted x-rays from the two sections interfere with each other to cause the observed doubled fringes.

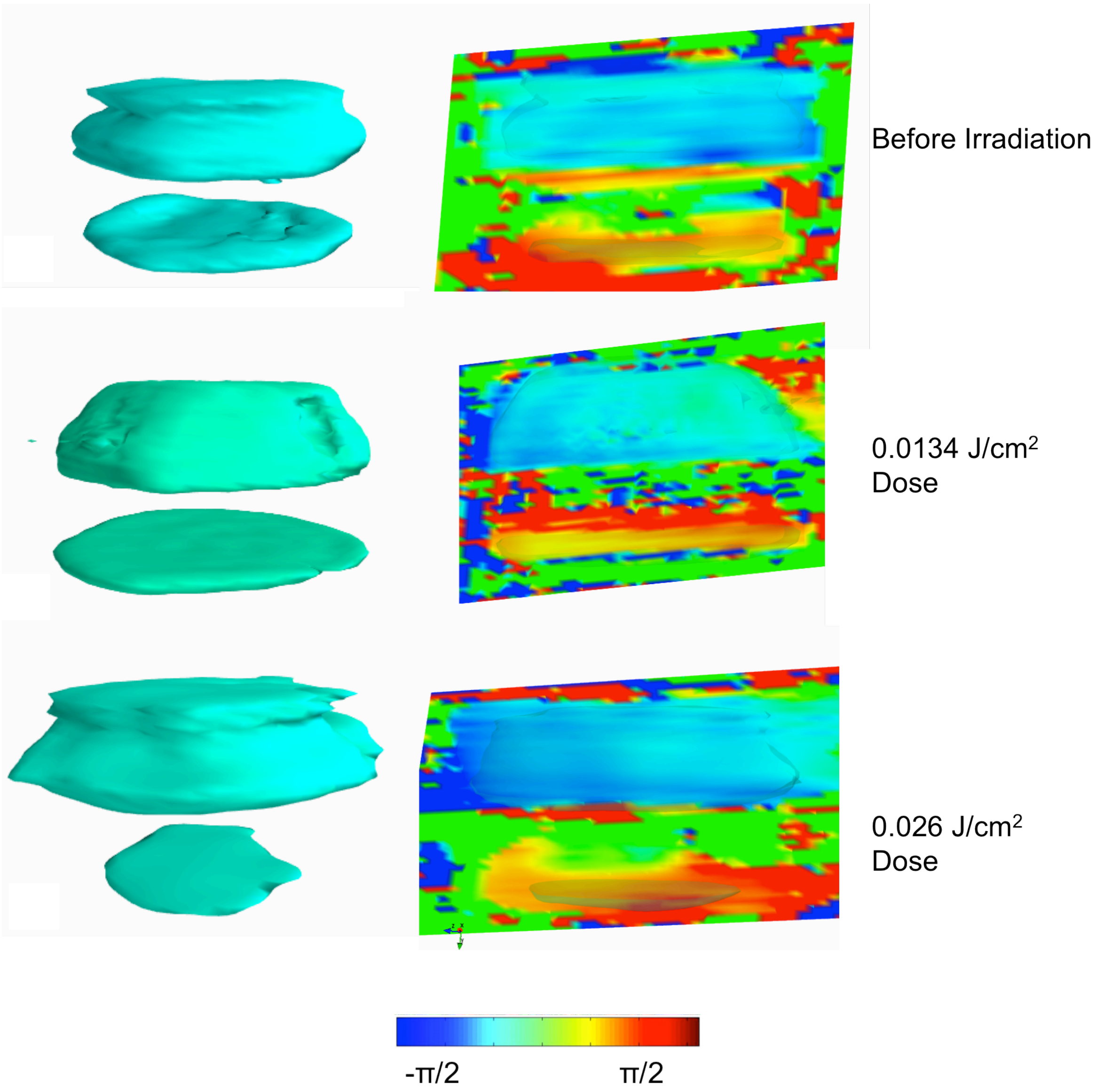

Figure 22. *Left images: Reconstructed complex amplitude (density) from irradiated crystal. Right: Recovered real space phase from irradiated crystal.*

Figure 21 shows the recovered real space phase as a scalar cut plane slice through the centre of the crystal. The colour indicates the phase value relative to another point on the phase map.

The recovered phase shows the predicted phase offset perfectly. It is clear that there is a phase difference between the upper to the lower slabs of the crystal. The overall difference in phase between the two pieces is π/2.

Comparison of the recovered real space amplitude reconstructions from the three doses levels is not particularly revealing. It is clear that there are differences, but nothing drastically conclusive. They all have a similar overall shape except that the before and 0.026 J/cm^2x10 show the same bulge in the upper portion, whereas the 0.026 J/cm^2 does not. Comparison of the before dose and 0.026 J/cm^2x10 reveals that the lower slab seems to have shrunk. Looking at the top view the 0.026 J/cm^2x10 reconstruction also appears to have developed a more pronounced bulge on the upper slab.

Summary

It was possible to measure a Bragg peak from a 200nm Au crystal, then remove the sample from the diffractometer, irradiate it with a laser and then find the Bragg reflection again for further measurement. This was made possible mostly as a result of the confocal alignment method, which has proven invaluable in experiments of this kind. It was possible to recover the real space phase and amplitude from the Bragg peak measurements in order to compare different laser doses with one another. It was found that the crystal contained a twin crystal or stacking faulted region in its centre. The phase offset predicted from diffraction patterns was observed in recovered phase. While no conclusive changes were observed as a result of laser irradiation, it was an important step in refining the methods used in this type of experiment. Since the preliminary experiment, another experiment of an XPP nature has been successfully carried out. One of the drawbacks in the first experiment was that the laser was not easily tuneable and was ex-situ, meaning changes could not be studied while measuring the Bragg reflection in real time. The results from the second experiment are promising and are still in preparation.

Visualising FIB induced damage with CXDI

Focused Ion Beam (FIB) is a technique used in areas such as materials science, the semiconductor industry and biology for deposition, ablation of materials and also as an imaging technique. The principle is the same as that used in scanning electron microscopy except that instead of a beam of electrons, an FIB used a beam of ions (often Gallium, but other materials are used). This beam of ions can be used to carve the most intricate patterns into a material and allows all kinds of structures to be produced. As a result of its widespread and numerous uses, understanding the precise nature of FIB induced damage is highly important.

We proposed to investigate localised ion beam induced strain in individual Au nanocrystals with CXDI. We damaged individual nanocrystals with a focused ion beam at varying doses to determine how strain develops at the surfaces of Au nanocrystals. We hoped to see the formation of various defects as a function of dosage (ion implantation, stacking fault, dislocation loop and other effects). By measuring each nanocrystal with CXDI before and after exposure to the FIB, we wanted to see the precise development of damage. Detailed SEM images were taken of each crystal at each stage to allow comparison with ‘phased’ reconstructions.

Experimental Method

A Carl Zeiss XB1540 “Cross-Beam” focussed-ion-beam microscope was used to perform the FIB damage. Crystals placed in the FIB were damaged in different ways in order to study various effects. The damage induced consisted of three main types: 1) Imaging damage – here the crystal to be damaged was imaged by the FIB in scanning mode so the entire surface of the crystal would receive a blanket dose; 2) Drilling – a very small area (around 20nm) hole was drilled into crystals right through to the substrate; 3) Sectioning – some crystals were effectively cut in half with the FIB.

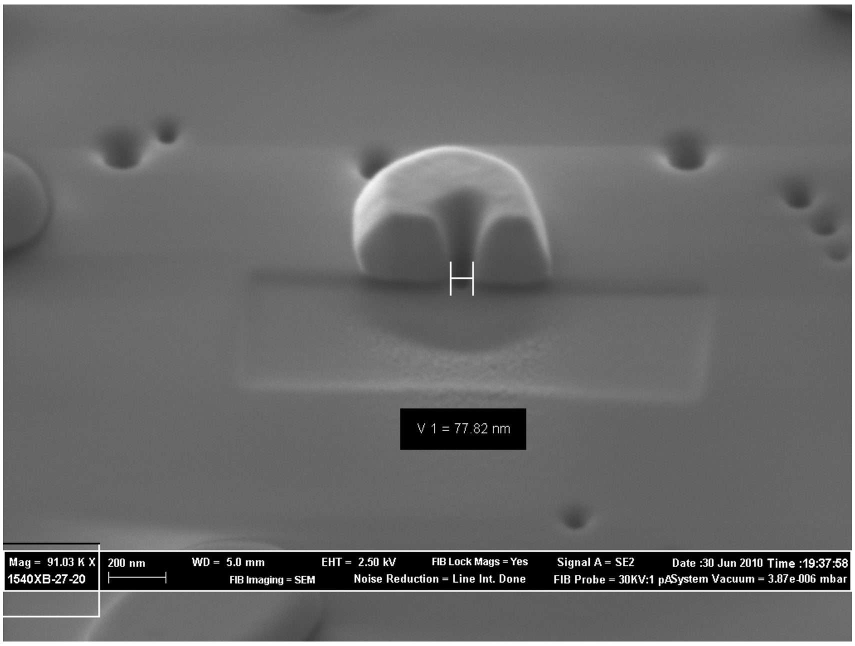

Figure 23. *SEM image of FIB milled crystal. In order to show damage profile it has then been 'sectioned' by cutting one half away.*

Measurements were made in the usual way as detailed in previous sections. A crystal of interest is brought into the known x-ray beam position using the confocal alignment method described earlier. The detector arm angles are now moved such that the desired Bragg reflection, once found, will appear squarely on the detector. Then the sample stage angle, θ is rotated step by step until a diffraction pattern is seen on the detector and a measurement can be made. The samples were placed at a high incidence angle of $\alpha = 8°$ throughout measurements and although multiple Bragg peaks were measured, the focus of this chapter will be on the $11\bar{1}$ reflection.

The diffraction patterns measured were reconstructed in order to recover the lost phase information and produce images of real space amplitude and phase. A background dataset was subtracted from the data to reduce the effects of noise in the data. Any cosmic rays were removed (provided they were not interfering with fringes). The data were binned with 2x2 binning in order to reduce computational time ensuring oversampling was maintained. Then phasing could be done. A threshold of 400 was applied to the intensity and the phase was constrained throughout computation to remain within $\pm\pi/2$. Shrinkwrap was used in order to create a tighter support and an example of a typical support can be seen in figure 20b. 200 iterations of pc-HIO were done followed by 10 ER iterations, then the shrinkwrap support was reformed followed by cycles of 10 pc-HIO, 2 ER iterations, support recalculation, 10 pc-HIO, 2 ER, support recalculation and so on until a solution was found.

Results

Figure 23 shows a selection of 2D intensity measurements through the centre of the Bragg peak. This particular dataset was constructed by summing 18 separate recordings of the Bragg peak together, in order to improve statistics. Each individual dataset was centred in its array and then added. Several features can be identified in the crystal by looking at its diffraction pattern alone. The very prominent fringes in the vertical axis correspond to the very strong top and bottom facets of the crystal. Some twinning can be seen in these vertical fringes indicating a missing section of crystal in the scattered rays from the crystal. This could either be that there is really a missing chunk taken out of the crystal, but it could also correspond to a section of crystal with a different crystallographic orientation to the rest, which this Bragg peak is not sensitive to. It can be seen that in the more central/brighter intensity slices, the background level appears to change from black to blue in colour. High readout levels on the detector are causing an unusual background level when the intensity is highest and is evidence of the imperfect nature of CCD detectors.

Figure 24 shows an SEM image of the same crystal. The crystal has been drilled into with the FIB at the top right corner as can be seen in the image. The crystal is of around 200nm in diameter and has a hexagonal type shape.

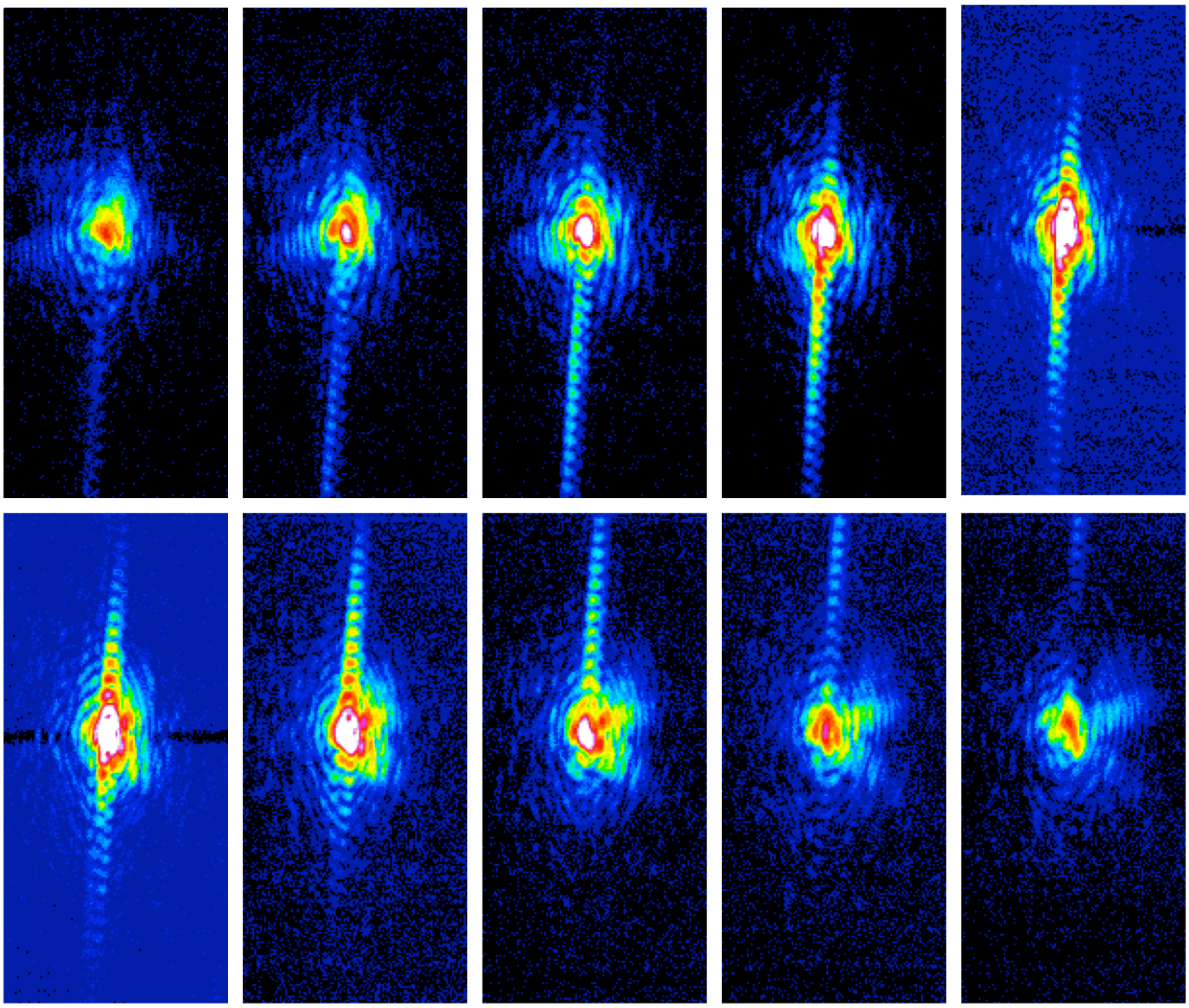

Figure 24. *A selection of 2D slices of intensity measurements from the Bragg peak of a 200nm Au crystal irradiated by FIB as shown in figure 24.*

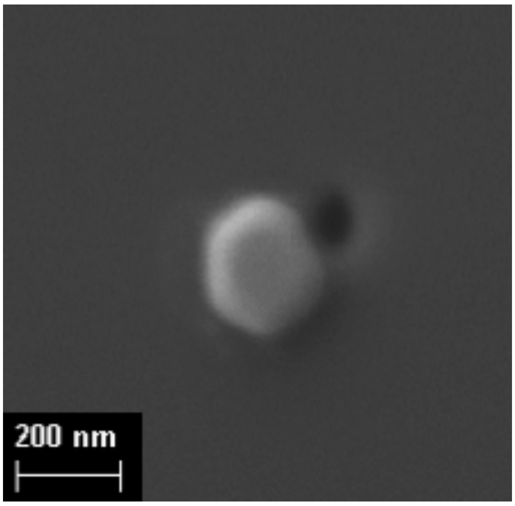

Figure 25. *An SEM image of an Au crystal after having been FIB milled at the top right corner.*

Figure 25 shows one of the reconstructions from a $11\bar{1}$ Bragg reflection intensity measurement. It is clear with comparison of a) and c) that the reconstructed real space amplitude reconstruction agrees strongly with the SEM images. The same shape is shown in the reconstruction and the same location of damage in SEM can also be seen. The damaged regions are circled in figures 25 a) and d) for clarity. It is clear that the FIB damage can be seen in the reconstructions and there are several patterns apparent in the recovered phase, which are likely due to the FIB milling. The bright blue spot at the top right part of the recovered phase shows a maximum phase shift in scattered rays of 5π/8 between the milled regions and unmilled regions of the crystal.

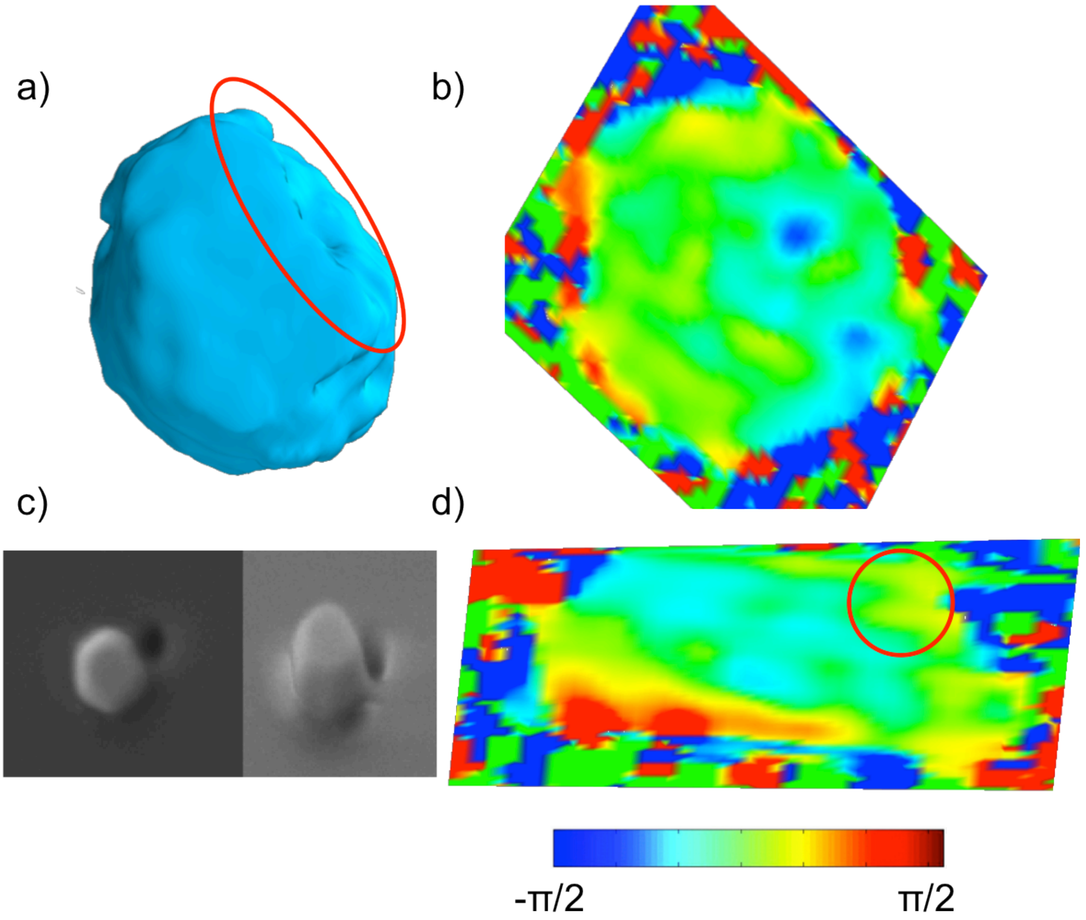

Figure 26. *a) Top view of reconstructed complex amplitude (density) of crystal after FIB milling b) Top view of recovered real space phase c) two SEM images showing FIB induced damage in Au crystal d) Side view of recovered real space phase.*

Summary

200nm sized Au crystals were successfully damaged with FIB, then imaged using CXDI and reconstructed successfully. In practice it was found to be difficult to limit the FIB exposure to a sufficiently small amount. Even on the lowest FIB energy setting, the focussed beam would cut through to substrate instantly and sometimes render the crystal unmeasurable with CXDI. The damage caused by FIB was shown in the reconstructed real space complex amplitude (density) and images were in strong agreement with SEM images. Recovered phase maps showed the maximum phase shift between sections next to milled region, to be a shift of $5\pi/8$ when compared with the non-milled regions.

Study of crystallographic imperfections with CXDI

If the stacking sequence of an fcc crystal is changed, the result will be a coherent twin boundary. Such twins are very common and may form either during crystal growth as ‘growth twins’/annealing twins or as a result of deformation. In order to investigate twin crystals with CXDI, a set of lithographically produced samples were made to encourage twin formation. A series of gold film dots of varying thicknesses were fabricated and once annealed at high temperature, it was hoped that the shape and size of the initial film deposit would influence crystal formation. A set of rhombus Au dots with a wide aspect ratio of 1:5, were used in order to promote twin growth. Additionally, triangle and hexagonal dots were also used.

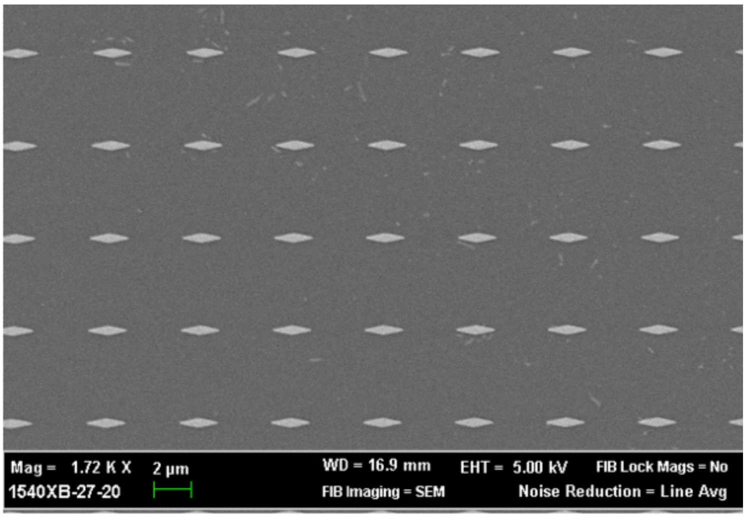

Figure 27. *SEM image of patterned Rhombus shaped Au film dots*

After sample preparation by high temperature heating over a period of 12 hours, the samples were ready for measurement. All measurements were carried out at beamline 34-ID-C of the APS. The same basic experimental procedure was followed as detailed in the previous chapters. The sample was placed on the detector and confocal alignment methods were used in order to determine precisely which crystals on the sample were imaged for later comparison with SEM images and to allow us to return to the same crystals multiple times. This also allowed measurement of multiple Bragg peaks enabling the construction of D-Fields.

Results

Figure 27 shows a reconstruction from a single Bragg peak measured from an Au nanocrystal. The crystal was formed from a Rhombus Au film dot upon annealing. A highly interesting hexagonal shaped crystal has been revealed which displays many interesting features. The shape of the crystal in figure 27a) is certainly unusual, as it has a kink in its lower facet with half a slice of missing amplitude located at the crystal substrate interface. Missing slices are fairly rare in CXDI measurements, and half a slice missing is even more so. The recovered phase pattern associated with the missing piece is no less interesting as evidenced by image b). A twin crystal, which has likely caused the section of missing amplitude in the reconstructions, has created a large phase shift in the boundary region corresponding to a significant ion displacement from the ideal lattice. A fascinating butterfly wing shaped strain field can be seen through the crystal as a result. A phase shift of π/3 can be seen at the substrate, crystal boundary interface as a result of the twin crystal's effects.

Whereas triangular Au film deposits will usually produce a single crystal, rhombus Au film shapes tend to produce multiple crystals. It is possible that the crystal imaged here is actually conjoined with a secondary crystal, part of which protrudes into the crystal shown in figure 27.

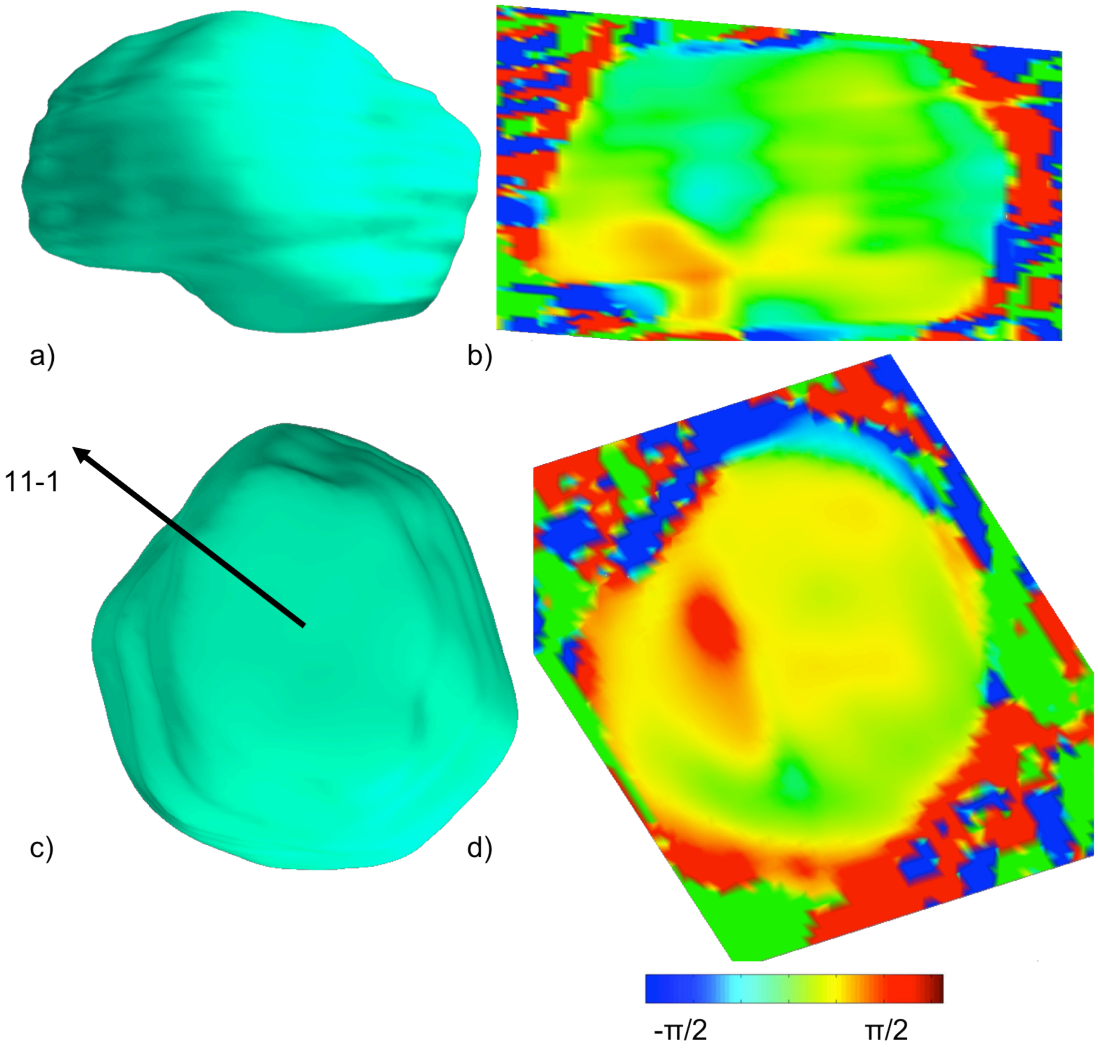

Figure 28. *Reconstructions from an Au nanocrystal: a) Side view of reconstructed complex amplitude (density) viewed as an Iso-Surface; b) Side view of recovered phase viewed as scalar-cut plane; c) Top view of reconstructed complex amplitude (density) viewed as Iso-Surface; d) Top view of recovered phase viewed as scalar-cut plane*

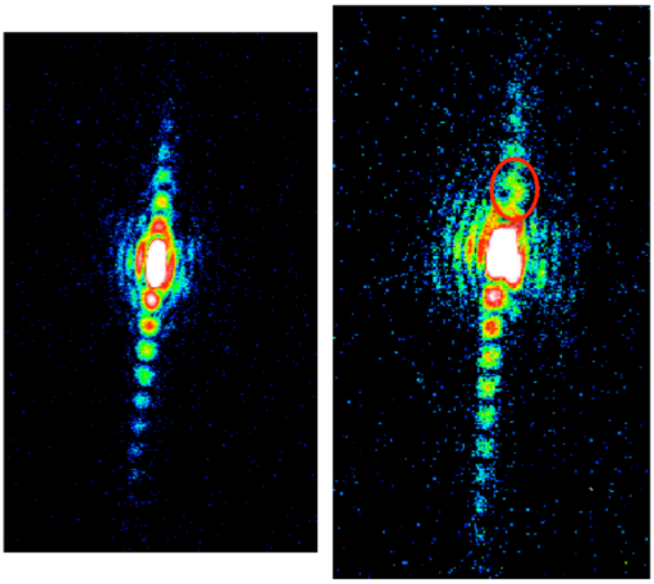

Figure 29. *2D intensity measurements from the same 200nm Au shown in figure 29 crystal: Left) central slice of 11-1 (left) Bragg reflection; Right) central slice of -111 (right) Bragg reflection*

Figure 28 shows slices through the intensity measurements from 11-1 and -111 Bragg reflections from the same 200nm Au crystal. The red encircled region in the right image, double fringes are present in the intensity pattern. This corresponds to a region from which the scattered x-rays are interfering with one another due to a phase offset between the two sections (this characteristic is indicative of a twin crystal). Interestingly it can be seen that the twin fringes are not present in the -111 reflection (left) from the same crystal. This was subsequently explained through analysis of the real space complex amplitude and phase.

Figure 29 shows the reconstructions from two Bragg reflections from the same crystal as in figure 28. Image a) is in very good agreement with the SEM image, e). The shape of the reconstruction is almost identical and has a very faceted morphology. Image c), the complex amplitude from the alternate reflection has a section of amplitude, which explains the double fringed diffraction pattern. The most likely explanation is that there is a twin crystal in the missing section, which the Q vector of the 11-1 Bragg reflection is not sensitive to. This in turn means the direction of reverse stacking in the twin crystal is perpendicular to the direction of the Q vector of the reflection measured. The existence of this twin is evidenced by close examination of the SEM image. A surface kink is visible, likely due to the twin piece of crystal further verifying its existence.

Image d) shows there to be a complex displacement pattern with a compression on one side and an expansion of the lattice on either side of the twin piece. The phase offset in the sections adjacent to the twin is around $\pi/2$.

We went back to the same crystal again in order to attempt to measure a Bragg reflection from the twin piece. A reconstruction of complex amplitude from the missing piece is shown in figure 30, in which the reconstructed piece can be seen to fit very well into the section of missing amplitude in the -111 reconstruction.

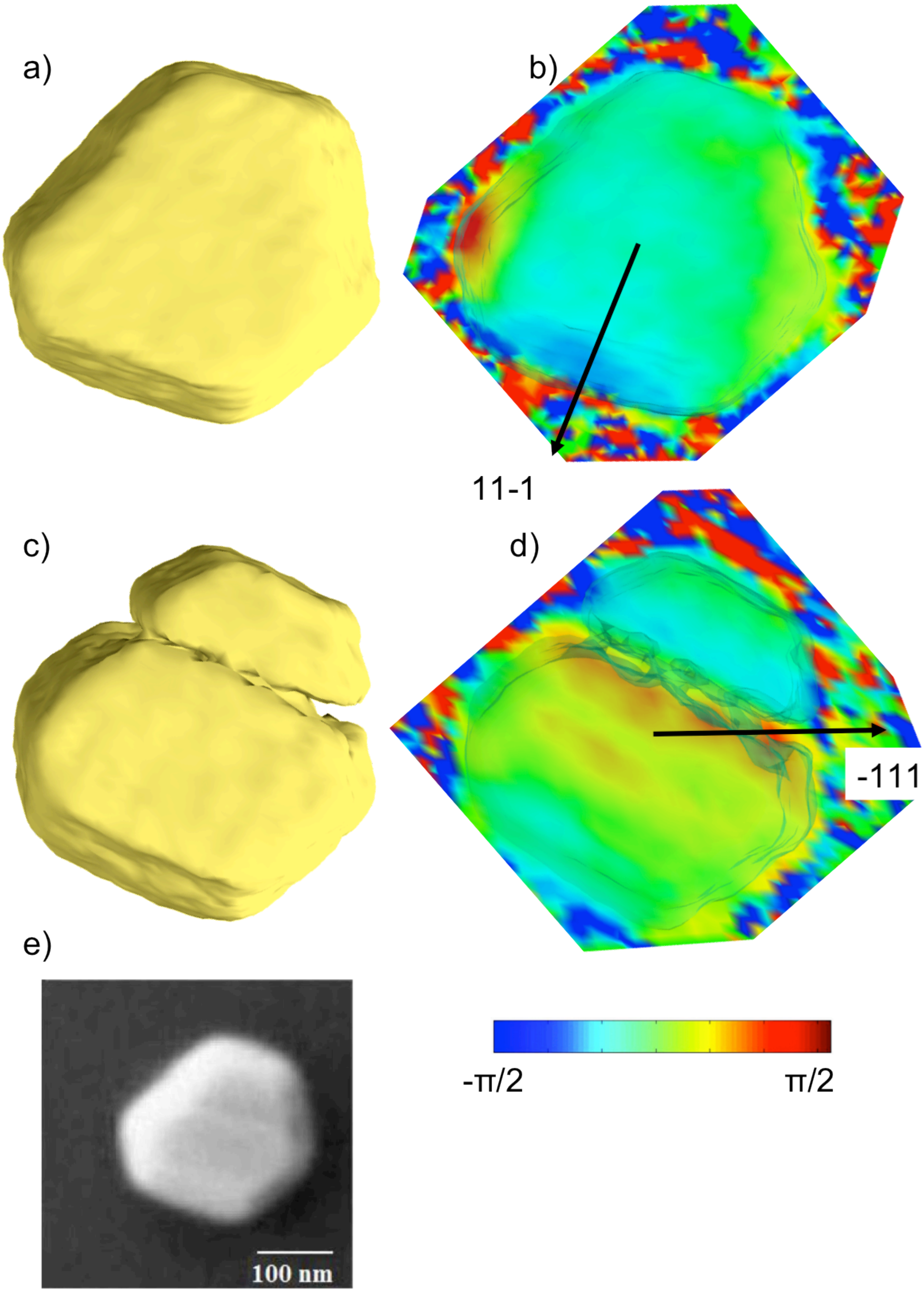

Figure 30. *Reconstructions from an Au nanocrystal with a twin crystal: a) Reconstructed real space complex amplitude (density) from 11-1 Bragg reflection viewed as an Iso-Surface; b) Recovered real space phase from Bragg 11-1 reflection of same crystal viewed as a scalar-cut plane; c) Reconstructed real space complex amplitude (density) from -111 Bragg reflection viewed as an Iso-Surface; d) Recovered real space phase from Bragg -111 reflection of same crystal viewed as a scalar-cut plane; e) SEM image of the same crystal as reconstructed in a-d).*

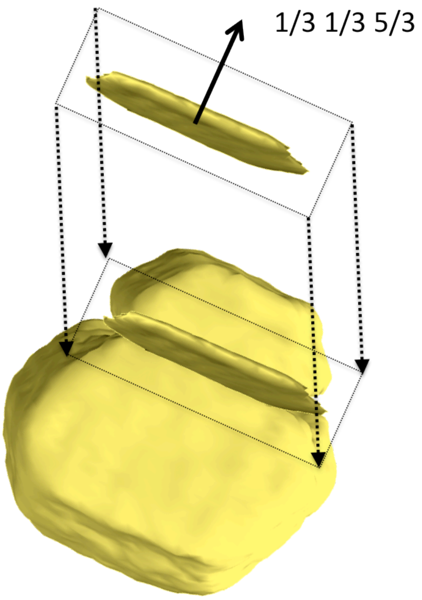

Figure 31. *Image demonstrating how a fractional Bragg reflection can be used to fill in a missing section of amplitude (due to twin) in a reconstruction*

Displacement field from three Bragg reflections

As discussed earlier on, one Bragg reflection can reveal one component of displacement along the direction of the Q-vector. So, by combining multiple reflections it is possible to build a displacement field. This was done using the reconstructions from the [11-1], [-111], and [020] reflections from the crystal shown in figures 28, 29 and 30 and the D-Field can be seen in figure 31.

In order to construct the images, the recovered phases from each of the three datasets were aligned with one another (rotated and translated), then the data were re-sampled (so that they were all in the same coordinate frame) and the phases interpolated. The resulting D-field was then aligned with an Isosurface image from the -111 Bragg reflection reconstruction of complex amplitude for visualisation purposes.

The D-field shows a set of many coloured arrows, which correspond to a displacement magnitude. The larger and further along a blue-red scale the arrows lie, the greater the lattice displacement within the crystal. The pattern of displacement magnitudes either side of the ‘missing piece’ or twin crystal, corresponds to a mean displacement in the downward direction on the left of the twin (looking at images a and b), and a mean upward displacement on the right hand side.

The displacement pattern visible on the far right hand edge of the crystal is unexplained and requires further investigation.

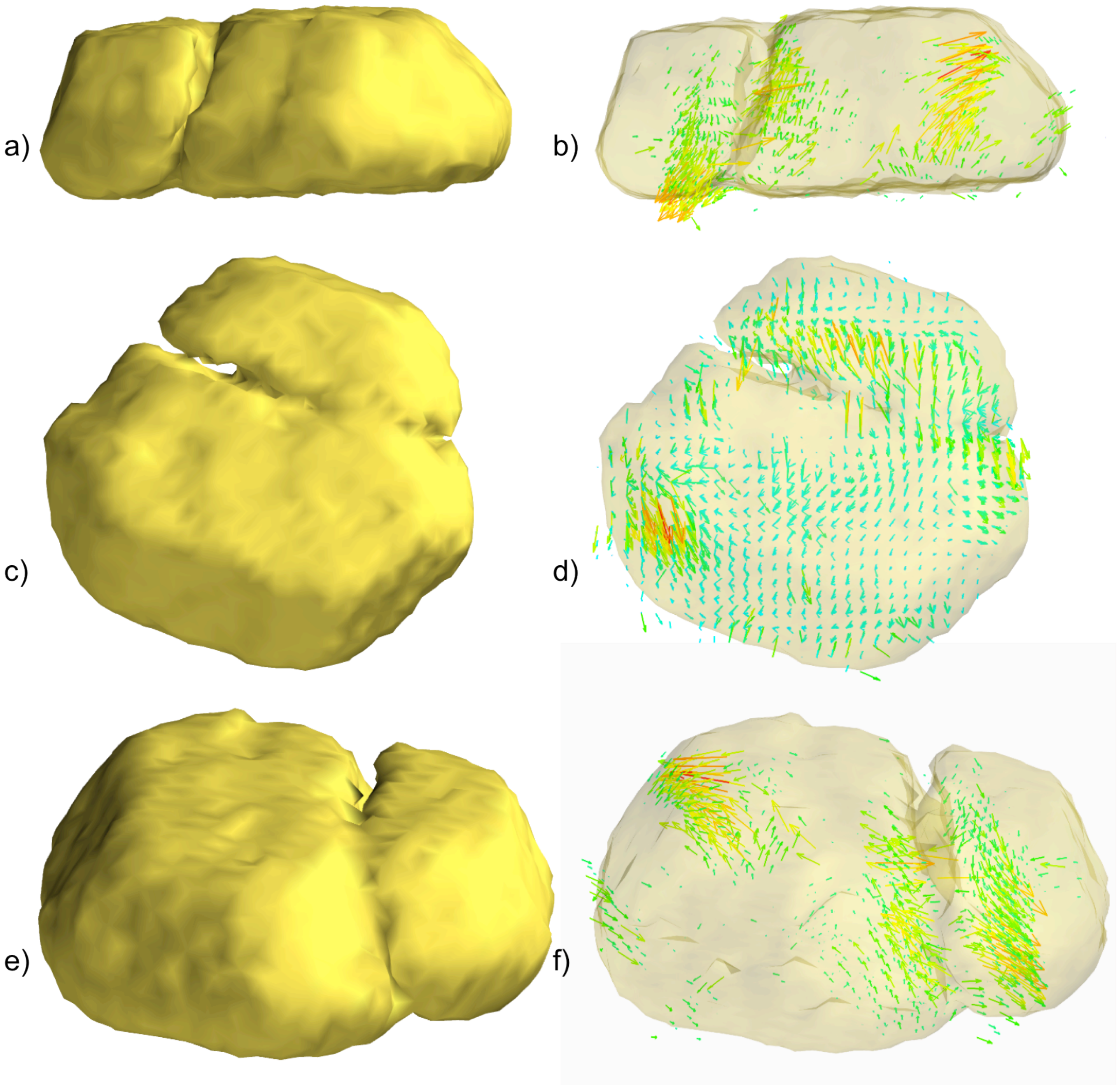

Figure 32. *Displacement field generated from three Bragg reflections from a single 200nm Au crystal. Left images) different views (side, top, profile) of reconstructed complex amplitude (density) viewed as Iso-Surfaces; Right images) different views (side, top, profile) of displacement field viewed as magnitude dependent arrows.*

Summary

Crystals with multiple stacking faults and twinned sections of reverse stacking were successfully imaged. Recovered complex amplitude shape and size of 200nm Au crystals has been found to be in close agreement with SEM images. A twin crystal seen in reconstructions was verified to exist through the presence of a surface kink visible in SEM images. Fascinating images of real space phase have been recovered revealing reasonable displacement patterns. 9 Bragg peaks have been measured from a single 200nm diameter Bragg peak. Three Bragg peaks were measured from a 30nm x 180 nm x 50 nm twin crystal contained within a larger 200nm crystal (which was also measured). These Bragg peaks were successfully inverted to provide real space amplitude and phase images. Multiple Bragg peaks from a single crystal were used to construct a Displacement field.

Chapter 6 - Conclusions

Materials on the nanoscale exhibit a dazzling array of unusual properties worthy of further investigation. The scientific search for answers in this realm can reveal a vast amount of information, which can help us to understand the world around us.

CXDI has proven to be a reliable tool for examining the very nature of the nanoscale world, especially when applied to the structural study of nanocrystals. The method of CXDI was proven to be a valid technique for evaluating properties in crystals such as crystallographic imperfections and the effects when such crystals are exposed to extreme conditions e.g laser irradiation and FIB induced damage. Comparison of CXDI reconstructions with real world images has shown that both the shape and density properties and the displacement found within crystals, can be determined with the method.

The first experiment discussed in this report described attempts to measure Bragg reflections from 200nm Au crystals before and after different levels of exposure to an intense Nd: YAG laser. Bragg reflections from crystals were successfully measured prior to irradiation and also after laser three successive exposures of increased amounts. Through iterative computational methods were able to reconstruct real space images of complex amplitude and phase. As can be seen in figure 22, these images revealed there to be a phase offset between two pieces of crystal separated by a region in between of a different crystallographic alignment. This missing piece was likely a twin crystal or stacking faulted region. The real space amplitude images verified the accuracy of reconstructions as it showed many similarities in shape to an SEM image taken of the same crystal. Although comparison of reconstructions from different levels of exposure to the laser did not reveal any conclusive differences, the diffraction patterns measured did. Comparing figures 18 and 19 reveals that the bright intensity fringes in the vertical axis are washed out after laser irradiation. Additionally a drop in intensity of 55% was found after 0.026 J/cm^2x10 pulses exposure. The overall difference in phase between the two pieces was found to be π/2. Data from a recent x-ray pump probe (where a high power laser, incident upon sample is timed with x-ray imaging bunches) is currently still in analysis and will hopefully reveal more about the effects of laser irradiation of Au nanocrystals.

The second experiment discussed earlier was the investigation of FIB damage in Au nanocrystals with CXDI. Multiple Bragg peak intensity measurements were made of 200nm diameter FIB milled Au crystals. Subsequent reconstructions recovered real space amplitude and phase information allowing visualisation of the damage caused by FIB. When aligned to the same reference frame as SEM images, the damage visible in the recovered complex amplitude was in agreement with the location of FIB damage in SEM images. The size of the damaged region in reconstructions was much larger in size than the damage visible in SEM images. One possible explanation is that the effects on the crystal structure actually travels much further into the crystal than the SEM image would suggest.

The next experiment discussed attempted to study crystallographic imperfections on Au crystals (likely caused by annealing). Figure 28 shows the reconstructed complex amplitude and phase from one crystal in particular. The images show an interesting missing section in the bottom half of the crystal. The images of recovered phase information show a large phase shift in the regions surrounding the missing piece. This reveals there to be a significant ion displacement from the ideal lattice as a result. A phase shift of around π/3 can be seen between the areas adjacent to the missing piece and the rest of the crystal. The crystal imaged was from a sample consisting of a series of Rhombus shaped Au dots, high temperature annealed in order to form crystals. It has been found that rhombus film dots tend to create multiple crystals, some of which appear conjoined in SEM images. One possible explanation for the shape of the reconstruction is that the crystal is conjoined with a twin crystal with different crystallographic alignment, which is protruding into the lower half of the imaged crystal.

Multiple Bragg peaks were successfully measured from one Au crystal in particular, which turned out to be an exceptionally interesting crystal. Reconstructions were found to agree uncannily with SEM images of the same crystal. The reconstructed complex amplitude and phase revealed the crystal to contain a thin section of crystal with reverse stacking (figures 30 and 31) present in reconstructions as a missing section of amplitude. This missing section corresponded to a kink observed on the surface of the crystal in SEM images. The reverse stacking idea was evidenced by the fact that one Bragg reflection did not show the missing piece at all, whereas other reconstructions showed very clearly a missing slice in the reconstructed real space amplitude. The likely explanation for this is that the Q vector direction of two out of three of the reflections measured, rendered them insensitive to the missing piece due to its crystallographic orientation. One reflection however, was sensitive to the crystallographic planes of the missing piece, so in reconstructions from this Bragg reflection, the missing piece appears filled in. It was possible to measure three Bragg reflections solely from the reverse stacked section. Only one of these reflections allowed a good reconstruction of real space complex amplitude and phase. Images of the reconstructed real space amplitude showed that indeed, it was a small piece of crystal of 20nm x 50nm x

200nm in size, which appeared to fit perfectly into the missing pieces seen in reconstructions from the bulk crystal.

Three Bragg reflections from the bulk crystal were then used to create a displacement field, allowing all three components of displacement inside the crystal to be resolved. Figure 32 shows the displacement field visually. The precise pattern of displacement magnitudes found either side of the 'missing piece' is very interesting. It shows a mean displacement downwards on one side of the missing piece and upwards on the other. The section of reverse stacking was found to cause a large amount of displacement. Results from this are still being interpreted.

Sample preparation revealed a great deal about how crystals form when annealed from a series of small film dots on a substrate. It was found that crystals tend to align to the edges of triangular and hexagonal shaped film dots. This makes patterned samples extremely useful in CXDI as it reduced the time necessary to locate a Bragg peak from a crystal. When used in conjunction with the confocal alignment methods described earlier, patterned samples allow crystals measured with coherent x-rays to be found at a later date with conventional microscope methods to compare reconstructions with 'real world' images. They also enable multiple Bragg reflections to be measured from a single nanocrystal.

Chapter 7 – Future work

For the remainder of the time available during my PhD, there are several things which I intend to do to continue this research.

Recently, a new type of much more time efficient, lower noise detector has been used in experiments – a ‘Pilatus’ detector. One of the main barriers previously was that a crystal would shift out of alignment after one or two hours, reducing the statistics attainable in a measurement. Using the Pilatus, we save roughly a factor of 4 in time, allowing much higher resolution data to be measured. One of my intentions is to return to several crystals in order to remeasure data with the Pilatus detector.

Further analysis of FIB data:

- Provided beamtime is available at the APS I wish to return to the FIB samples and create some new ones to look at. Unfortunately, datasets were not measured before FIB damage, so it would be extremely useful to measure several crystals prior to being damaged, then return to study the FIB effects.
- Additionally, multiple Bragg reflections were measured of one crystal which had been FIB damaged. I intend to create a displacement field from these data in order to resolve the three components of displacement

Laser irradiation and XPP (x-ray pump probe) experiments:

- I feel that more has yet to be revealed from the laser irradiation experiment. Further analysis of these data could potentially reveal an effect of the laser irradiation, which was not revealed in the reconstructions shown in this report.
- I would also like to return and expose the same crystal measured before, to a higher power laser which could potentially cause re-crystallisation of crystals, provided high enough power is reached.
- A recent XPP experiment was carried out at 7-ID of the APS. Data from this experiment are still to be fully analysed. The data recorded in this experiment were very high resolution, as the Pilatus detector was used. The reconstructions from this experiment could potentially be extremely interesting and could reveal a great deal about the time dependant nature of laser induced heating in nanocrystals.

Study of crystallographic imperfections in Au

- There are several crystals not mentioned in this report, which have provided extremely interesting reconstructions and warrant further investigation. I intend to return to some of these crystals in order to measure high resolution and multiple Bragg peak data
- The reconstructions from crystals shown in figures 28 and 30 are still not fully understood and require a great deal more investigation to fully understand the results.

Future x-ray free electron laser experiment

- Our group received remarkable news, which is that we have been allocated beamtime at one of the most exciting new scientific facilities in the world; the LCLS in Stanford (linear coherent light source). This light source is capable of producing a vastly more bright (than synchrotrons), extremely coherent femtosecond x-ray beam for the study of materials.
- We will perform an XPP experiment, where a powerful laser is synchronised with the x-ray imaging pulses enabling the time dependant nature of laser induced shock waves to be studied. By varying the laser to x-ray pulse timing offset, we hope to be able to image shock waves propagating through a 200nm Au crystal

References

1. Schmidbaur, H., et al., *Understanding gold chemistry through relativity.* Chemical Physics, 2005. **311**(1-2): p. 151-161.
2. Chemistry, R.S.o. *Gold - Au*. Available from: http://www.rsc.org/chemsoc/visualelements/pages/data/gold_data.html.
3. *Gold – Applications and Developments in the Electronics, Biomaterials and Catalysis.* Materials World, 2003. **11**(2): p. 12-14.
4. Paciotti, G.F., et al., *Colloidal Gold: A Novel Nanoparticle Vector for Tumor Directed Drug Delivery.* Drug Delivery, 2004. **11**(3): p. 169-183.

5. Krpetic, Z., F. Porta, and G. Scarì, *Selective entrance of gold nanoparticles into cancer cells.* Gold Bulletin, 2006. **39**(2): p. 66-68.

6. Hutchings, G., *Catalysis by gold.* Catalysis Today, 2005. **100**(1-2): p. 55-61.

7. Haruta, M., et al., *Novel gold catalysts for the oxidation of carbon monoxide at a temperature far below 0 C.* Chemistry Letters, 1987. **16**(2): p. 405-408.

8. Nkosi, B., N. Coville, and G. Hutchings, *Vapour phase hydrochlorination of acetylene with group VIII and IB metal chloride catalysts.* Applied catalysis, 1988. **43**(1): p. 33-39.

9. Langley, R., *Gold Coatings for Temperature Control in Space Exploration.* Gold Bull, 1971. **4**(4): p. 62-66.

10. Maeland, A. and T. Flanagan, *X-Ray and Thermodynamic Studies of the Absorption of Hydrogen by Gold-Palladium Alloys.* The Journal of Physical Chemistry, 1965. **69**(10): p. 3575-3581.

11. Tuckerman. *Unit cells and the crystal structure*. 2007; Available from: http://www.nyu.edu/classes/tuckerman/honors.chem/lectures/lecture_20/node2.html.

12. Ibach, *Physics of Surfaces and Interfaces*2006.

13. Callister, *Materials Science and Engineering, an Introduction*2007.

14. Volkert, C.A. and E.T. Lilleodden, *Size effects in the deformation of sub-micron Au columns.* Philosophical Magazine, 2006. **86**(33-35): p. 5567-5579.

15. Verhoeven, *Fundamentals of Physical Metallurgy*1975.

16. Grosskreutz, J., C. Bowles, and A. Wahab, *Observations of slip patterns on the surface of fatigued gold using the scanning tunnelling microscope.* Journal of Materials Science, 1992. **27**(21): p. 5756-5764.

17. Li, Y.P., et al., *Direct observation of dislocation plasticity in 100 nm scale Au/Cu multilayers.* Applied Physics Letters, 2007. **91**(6): p. 061912.

18. Melbourne, S.o.E.S.-T.U.o. *Critical resolved shear stress*. 1999; Available from: http://web.earthsci.unimelb.edu.au/wilson/ice1/criticalrss.html.

19. Pimpinelli, *Physics of Crystal Growth.* 1998.

20. Yamada, *Equation of State for Free Energy of Homogeneous Nucleation in Supersaturated Lennard-Jones Vapor Phase Derived by Monte Carlo Simulations*.

21. Bragg, W. and W. Bragg, *The reflection of X-rays by crystals.* Proceedings of the Royal Society of London. Series A, Containing Papers of a Mathematical and Physical Character, 1913. **88**(605): p. 428-438.

22. Als-Nielsen, J. and D. McMorrow, *Elements of Modern X-Ray Physics*2001: Wiley.

23. Brauer, S., G.B. Stephenson, and M. Sutton, *Perfect Crystals in the Asymmetric Bragg Geometry as Optical Elements for Coherent X-ray Beams.* Journal of Synchrotron Radiation, 1995. **2**(4): p. 163-173.

24. Robinson, I.K., *Optimisation of coherent X-ray diffraction imaging at ultrabright synchrotron sources.* Zeitschrift f¸r Kristallographie Supplements, 2009. **2008**(27): p. 27-35.

25. Veen, F.v.d. and F. Pfeiffer, *Coherent x-ray scattering.* Journal of Physics: Condensed Matter, 2004. **16**(28): p. 5003-5030.

26. Robinson, I.K., et al., *Enhancement of coherent X-ray diffraction from nanocrystals by introduction of X-ray optics.* Opt. Express, 2003. **11**(19): p. 2329ñ2334.

27. Xiong, G., et al., *Coherent x-ray diffraction imaging of ZnO nanostructures under confined illumination.* New Journal of Physics, 2011. **13**: p. 033006.

28. Vartanyants, I. and I. Robinson, *Partial coherence effects on the imaging of small crystals using coherent X-ray diffraction.* Journal of Physics: Condensed Matter, 2001. **13**: p. 10593.

29. Newton, M., et al., *Three-dimensional imaging of strain in a single ZnO nanorod.* Nature Materials, 2009. **9**(2): p. 120-124.

30. Beitra, L., et al. *Confocal Microscope Alignment of Nanocrystals for Coherent Diffraction Imaging*. 2010.

31. Sayre, D., *Some implications of a theorem due to Shannon.* Acta Crystallographica, 1952. **5**(6): p. 843.

32. Harder, R., et al., *Imaging of complex density in silver nanocubes by coherent x-ray diffraction.* New Journal of Physics, 2010. **12**(3): p. 035019.

33. Shannon, C.E., *Communication in the Presence of Noise.* Proceedings of the IRE DOI -, 1949. **37**(1): p. 10-21.

34. Millane, R., *Multidimensional phase problems.* Journal of the Optical Society of America A, 1996. **13**(4): p. 725-734.

35. Miao, J., D. Sayre, and H.N. Chapman, *Phase retrieval from the magnitude of the Fourier transforms of nonperiodic objects.* J. Opt. Soc. Am. A, 1998. **15**(6): p. 1662-1669.

36. Leake, S.J., et al., *Longitudinal coherence function in X-ray imaging of crystals.* Opt. Express, 2009. **17**(18): p. 15853-15859.

37. Leake, S.J., *Coherent X-ray Diffraction Imaging of Zinc Oxide Crystals*, 2010.

38. Robinson, I. and R. Harder, *Coherent X-ray diffraction imaging of strain at the nanoscale.* Nature Materials, 2009. **8**(4): p. 291-298.

39. Fienup, J.R., *Reconstruction of a complex-valued object from the modulus of its Fourier transform using a support constraint.* J. Opt. Soc. Am. A, 1987. **4**(1): p. 118-123.

40. Vartanyants, I., et al., *Reconstruction of surface morphology from coherent x-ray reflectivity.* Physical Review B, 1997. **55**(19): p. 13193-13202.

41. Robinson, I., et al., *Reconstruction of the Shapes of Gold Nanocrystals Using Coherent X-Ray Diffraction.*

42. Miao, J., et al., *High Resolution 3D X-Ray Diffraction Microscopy.* Physical Review Letters, 2002. **89**(8): p. 088303.

43. Williams, G., et al., *Three-Dimensional Imaging of Microstructure in Au Nanocrystals.* Physical Review Letters, 2003. **90**(17): p. 175501.

44. Fienup, J., *Phase retrieval algorithms: a comparison.* Applied Optics, 1982. **21**(15): p. 2758-2769.

45. Bauschke, H.H., P.L. Combettes, and D.R. Luke, *Phase retrieval, error reduction algorithm, and Fienup variants: a view from convex optimization.* JOSA A, 2002. **19**(7): p. 1334-1345.

46. Fienup, J., *Invariant error metrics for image reconstruction.* Applied Optics, 1997. **36**(32): p. 8352-8357.

47. Harder, R., et al., *Orientation variation of surface strain.* Physical Review B, 2007. **76**(11): p. 115425.

48. Chen, C., et al., *Application of optimization technique to noncrystalline x-ray diffraction microscopy: Guided hybrid input-output method.* PHYSICAL REVIEW-SERIES B-, 2007. **76**(6): p. 64113.

49. Marchesini, S., et al., *X-ray image reconstruction from a diffraction pattern alone.* Physical Review B, 2003. **68**(14): p. 140101.

50. Newton, M., *Supplementary Information.* 2009.

51. Bringa, E.M., et al., *Shock deformation of face-centred-cubic metals on subnanosecond timescales.* Nature Materials, 2006. **5**(10): p. 805-809.

52. Yang, B. and G. Chen, *Partially coherent phonon heat conduction in superlattices.* Physical Review B, 2003. **67**(19): p. 195311.